UNIVERSIDAD DE CONCEPCIÓN
FACULTAD DE CIENCIAS FÍSICAS Y MATEMÁTICAS

A TENTATIVE $\sim$1000 km s^{-1} OFFSET BETWEEN THE [CII] 158 μm AND Lyα LINE EMISSION IN A STAR-FORMING GALAXY AT $z = 7.2$

Por: Raúl Hernán Baier Soto

Tesis presentada a la Facultad de Ciencias Físicas y Matemáticas de la Universidad de Concepción para optar al grado académico de Magíster en Ciencias con Mención en Física

Marzo 2022

Concepción, Chile

Profesor Guía: Rodrigo Herrera-Camus

Dedicado a todos mis seres queridos.

AGRADECIMIENTOS

Agradezco el apoyo y trabajo brindado por el Partner Group "The Baryon Cycle in Galaxies" entre la Universidad de Concepción y el Instituto Max Planck (MPE), liderado por mi profesor guía, Dr. Rodrigo Herrera-Camus.

A los profesor de la comisión evaluadora, Dr. Rodrigo Reeves y Dr. Stefano Bovino, quienes han tenido la disponibilidad, compromiso y dedicación durante todo el tiempo de mi investigación.

Al profesor Julio Oliva, director del programa de Magíster en Ciencias con mención en Física, quien ha cumplido una labor excepcional durante todo el tiempo que he sido parte del programa.

Finalmente, a toda mi familia; siempre han estado ahí apoyándome.

Resumen

Keywords – galaxias, alto redshift, evolución de galaxias

GN-108036 es una galaxia típica a $z = 7.213$, y es una de las fuentes conocidas más distantes del hemisferio norte. Basado en observaciones del telescopio NOrthern Extended Millimeter Array (NOEMA), reportamos la detección tentativa de la línea [CII] 158 μm con un nivel de significancia de 3σ. La emisión integrada de la línea no coincide espacialmente por ~ 4 kpc respecto de la emisión UV en reposo. La luminosidad total de [CII] ($L_{[\mathrm{CII}]} = 2.7 \times 10^8\ L_\odot$) es consistente con la relación entre luminosidad de [CII] y tasa de formación estelar (SFR) observada en galaxias cercanas y también en galaxias a alto redshift. Más interesante, la línea [CII] está corrida hacia el azul respecto a la línea Lyα por 982.2 ± 12.7 km s^{-1}. Si se confirma, este corresponde al valor más alto en diferencia de velocidad entre la línea Lyα y una línea no resonante reportada hasta ahora a $z \gtrsim 6$. De acuerdo a las tendencias observadas en otras galaxias a alto redshift, el gran valor de diferencia en velocidad en GN-108036 es consistente con su bajo ancho equivalente de Lyα y su alta magnitud absoluta UV. Basado en modelos de transferencia radiativa de la emisión Lyα de cáscaras que se expanden, la gran diferencia de velocidad puede ser interpretada como una gran densidad de columna de gas de hidrógeno, o viento galáctico con una velocidad de $v_{\mathrm{out}} \sim \Delta v_{\mathrm{Ly}\alpha}/2 \sim 500$ km s^{-1}. Tabmién reportamos la potencial detección (3σ) de un sistema compañero localizado ~ 30 kpc al este de GN-108036, a una similar velocidad sitémica y sin una contraparte en la emisión UV en reposo.

Abstract

Keywords – galaxies, high redshift, galaxy evolution

GN-108036 is a star-forming galaxy at $z = 7.21$, and one of the most distant known sources in the Northern hemisphere. Based on observations from the NOrthern Extended Millimeter Array (NOEMA), here we report the tentative detection of the [CII] 158 μm line at 3σ significance. The integrated [CII] line emission is spatially offset about ~ 4 kpc from the rest-frame UV emission. The total [CII] luminosity ($L_{[\rm CII]} = 2.7 \times 10^8\ L_\odot$) is consistent with the relation between [CII] luminosity and star formation rate (SFR) observed in nearby and high-z star forming galaxies. More interestingly, the [CII] line is blueshifted with respect to the Lyα line by 982.2 ± 12.7 km s^{-1}. If confirmed, this corresponds to the largest velocity offset reported to date between the Lyα line and a non-resonant line at $z \gtrsim 6$. According to trends observed in other high redshift galaxies, the large Lyα velocity offset in GN-108036 is consistent with its low Lyα equivalent width and high UV absolute magnitude. Based on Lyα radiative transfer models of expanding shells, the large Lyα velocity offset in GN-108036 could be interpreted as the presence of a large column density of hydrogen gas, or an outflow with a velocity of $v_{\rm out} \sim \Delta v_{{\rm Ly}\alpha}/2 \sim 500$ km s^{-1}. We also report the 3σ detection of a potential galaxy companion located ~ 30 kpc east of GN-108036, at a similar systemic velocity, and with no counterpart rest-frame UV emission.

Contents

AGRADECIMIENTOS **i**

Resumen **ii**

Abstract **iii**

1 Introduction **1**
1.1 Very high-redshift galaxies . . . 1
1.1.1 What is a very high-z galaxy? . . . 1
1.1.2 Why study high-z galaxies? . . . 2
1.1.3 How to study very high-z galaxies? . . . 3
1.2 Galaxias a muy alto redshift . . . 4
1.2.1 ¿Qué es una galaxia a muy alto redshift? . . . 4
1.2.2 ¿Por qué estudiar galaxias a muy alto redhsift? . . . 4
1.2.3 ¿Cómo estudiar galaxias a muy alto redshift? . . . 5

2 Theoretical Framework **6**
2.1 Lyα emission . . . 6
2.1.1 Lyα observations in high-z galaxies . . . 6
2.2 [CII] 158 μm transition . . . 8
2.2.1 [CII] 158 μm - FIR ratio . . . 9
2.2.2 [CII] 158 μm at $z > 6$ . . . 10
2.2.3 Star formation rate - [CII] luminosity relation . . . 10
2.3 [CII] 158 μm - Lyα offsets . . . 12
2.3.1 Lyα - [CII] spatial offset . . . 12
2.3.2 Lyα - [CII] velocity offset . . . 13

3 Methodology and Results **17**
3.1 Observations and data reduction . . . 17
3.1.1 Target . . . 17
3.1.2 NOEMA interferometer . . . 18
3.1.3 NOEMA observations . . . 20
3.1.3.1 Dust continuum . . . 20
3.1.4 Tentative detection of the [CII] 158 μm transition in GN-108036 . . . 22

4 Analysis **25**
4.1 Relation between [CII] line emission and star formation activity . 25
4.2 Lyα - [CII] velocity offset 26

5 Conclusions **29**

References **33**

Appendix **42**

A NOEMA [CII] line observations of GN-108036 **42**

List of Tables

3.1.1 [CII] 158 μm fluxes and parameters from the Gaussian fit to the tentative detections of GN-108036 and its companion 22

List of Figures

1.1.1 Scheme of the first galaxies assembly. In this case, the first galaxies reside in atomic cooling halos and their masses are in the order of $\sim 10^8$ $M_\odot$ and collapse at $z \sim 10$. Here the mini halos that house the first stars (Pop III) formed earlier ($z \sim 20$) are not considered as galaxies. Figure adapted from Bromm and Yoshida (2011). . . 2
1.1.2 Cosmic reionization process as a function of z. Simulation of the [HI] 21 cm emission considering radiative transference. Figure adapted from Thomas et al. (2009). 3

2.1.1 Prominent two Lyα detections of SDF-63544 (left) and SDF-46975 (right). The top panels show the composite two-dimensional spectra of both galaxies. Figure adapted from Ono et al. (2011). 7
2.1.2 Lyα line emission in a sample of 36 galaxies at $z > 6$ detected using the Lyman break drop-out technique. Figure adapted from Ning et al. (2021) 8
2.2.1 [CII] 158 mμ line to FIR continuum rate for different types of galaxies and also for high-z systems ($z > 1$) against FIR luminosity. Figure adapted from (Herrera-Camus et al., 2018) 9
2.2.2 Highest significance ($\geq 7\sigma$) levels of detection in the REBELS large program. Figure adapted from Bouwens et al. (2021). 11
2.2.3 $\Sigma_{\rm SFR}$ and $\Sigma_{\rm [CII]}$ scaling relation using different SFR tracers. In all panels m, N and σ indicate the slope of the relation, y-axis value at $x = 40$ and the standard deviation in dex, respectively. Figure adapted from Herrera-Camus et al. (2015) 12
2.3.1 Spatial offset between Lyα + UV (grey scale), [CII] (red contours) and [OIII] emission. Figure adapted from Carniani et al. (2018) . 13
2.3.2 Simulation of a primeval galaxy at $z \sim 7$. Figure adapted from Maiolino et al. (2015). 14
2.3.3 Schematic representation of the expected Lyα and non-resonant photons (e.g., [CII] or [OIII]) if the gas in the blobs surrounding the galaxy is static (top), inflowing (middle) and outflowing (bottom). The solid blue and red dotted line represent the Lyα emission and non-resonant line, respectively. Figure adapted from Yang et al. (2014). 14

2.3.4 Compilation by Hashimoto et al. (2019) of $\Delta v_{\mathrm{Ly}\alpha}$ as a function of Lyα equivalent width (left), absolute UV magnitude (center), and [CII] luminosity for high-z galaxies ($z \sim 6-8$). In all three panels N, ρ and p indicates the number of individual data points, the Spearman rank correlation coefficient for each relation and the probability satisfying the null hypothesis, respectively. Figure adapted from Hashimoto et al. (2019) 16

3.1.1 Lyα spectral profile of GN-108036 obtained using the DEep ImagingMulti-Object Spectrograph at the Nasmyth focus of the 10 meters Keck II telescope. Figure adapted from Ono et al. (2011). 18
3.1.2 HST rest-frame UV map of the field of GN-108036. Black circle indicates the position of the galaxy. 19
3.1.3 Seven antennas of the NOEMA observatory in the French Alps at 2550 meters above sea level. Credits: IRAM (www.iram-institute.org) 19
3.1.4 Instrumental tuning of NOEMA Band 3. 20
3.1.5 NOEMA dust continuum map of GN-108036 using the lower side band (LSB, $\nu_{\mathrm{restfreq}} = 218$ GHz) of the spectral window. Black solid contours are at levels of 1 and 2σ ($\sigma = 13$ μJy beam^{-1}). Dashed contours trace negative levels at -1 and -2σ. 21
3.1.6 *Left:* [CII] line spectrum of GN-108036 (top) and a potential companion located $\sim$ 30 kpc east (bottom). The zero velocity is set using the redshift from the detection of the Lyα line (black dashed vertical line Ono et al., 2011). The best 1D Gaussian fits to the tentative detections are shown in red. *Right:* HST rest-frame UV map of the field of GN-108036. The black dotted circle indicates the position of the HST rest-frame UV emission from GN-108036, and the black solid circle around the center has a radius of 30 kpc. The integrated intensity contours of the CII] line emission (2.5, 3, 4 and 5σ levels) are shown in magenta for the potential detection of GN-108036, and green for the potential companion. 23

4.1.1 [CII] luminosity $-$ SFR relation observed in $z \gtrsim 6$ galaxies (gray circles; Matthee et al., 2019). The solid (orange) and dot-dashed (blue) lines correspond to the scaling relations observed in star-forming galaxies on and above ($\times 20 - 100$) the main-sequence (Herrera-Camus et al., 2018). The tentative detection of GN-108036 is shown with a magenta diamond. The SFR of GN-108036 ranges from ≈ 30 to ≈ 100 M$_\odot$ year^{-1} depending if the rest-frame UV emission or SED are used, respectively (Ono et al., 2011). The green solid line indicates the [CII] luminosity for the companion, which does not have an HST counterpart or SFR estimate available. 26

4.2.1 Lyα velocity offset ($\Delta v_{Ly\alpha}$) with respect to the [CII] line as a function of Lyα equivalent width (*left*) and absolute UV magnitude (*right*) observed in star-forming galaxies at $5 < z < 8$ (gray circles; Hashimoto et al., 2019). The tentative detection (3σ) of GN-108036 is shown in both panels with a pink diamond. 28

A0.1 *Left:* NOEMA spectrum of GN-108036 with a possible new [CII] 158 μm transition detection (orange area). In all three panels, the green dotted line indicates the respective rms noise for three different data sets. Red solid line indicates the redshift measured by Lyα detection. *Right:* Same as the left panel but for the companion system. 42

A0.2 Flux map of GN-108036 in [CII] emission line for the compact data set. The contours corresponds to the 2.5σ, 3σ, 3.5σ, 4σ, 4.5σ, 5σ and 5.5σ (integrated) levels. The beam size is plotted in the bottom left. 43

Chapter 1

Introduction

1.1 Very high-redshift galaxies

This project focuses on the study of the interstellar medium (ISM) properties and environment of a star-forming galaxy near the epoch of reionization, i.e, at redshift (z) between 6 and 8. For this reason, it is necessary to begin by clarifying some key things in the study of very high-z systems.

1.1.1 What is a very high-z galaxy?

There is no simple answer for this question, in part because theoretical and observational point of views have different definitions, and also because technical developments change the definition as we detect systems further away.

From an observer perspective, a simple definition of very high-z galaxy corresponds to the highest redshift galaxy currently observed. Of course this definition changes with time and goes hand in hand with technological and technical development. A slightly more elaborate definition is a galaxy with a metallicity (Z) very close to zero (or zero), but this may be misleading because even the first galaxies could be already metal-enriched by super nova (SNe) triggered by the first stars (see Bromm and Yoshida, 2011).

For simplicity, in this work I will consider as a very high-z galaxy all sources at $z > 6$ detected to date. This is not a bad assumption, even more if we consider the cold dark matter (ΛCDM) cosmology, where structure forms hierarchically through

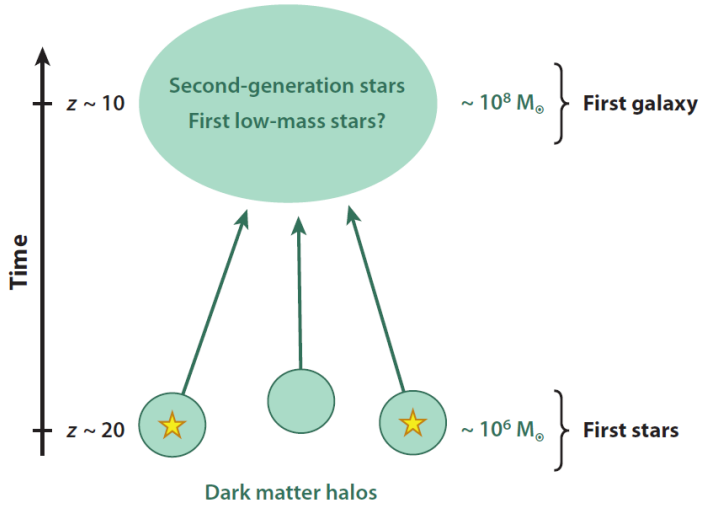

Figure 1.1.1: Scheme of the first galaxies assembly. In this case, the first galaxies reside in atomic cooling halos and their masses are in the order of $\sim 10^8$ $M_\odot$ and collapse at $z \sim 10$. Here the mini halos that house the first stars (Pop III) formed earlier ($z \sim 20$) are not considered as galaxies. Figure adapted from Bromm and Yoshida (2011).

mergers of smaller dark matter halos (DM). Figure 1.1.1 shows a representation of the first galaxies assembly, where the first galaxies at $z \sim 10$ formed through the collapse of mini halos dark matter at $z \sim 20$.

1.1.2 Why study high-z galaxies?

It is thought that the first galaxies were formed within the first $\sim$ 200-300 Myr of the Universe lifetime (e.g., Bromm and Yoshida, 2011; Wise et al., 2011). These systems are recognized as key drivers of early cosmic evolution, and represent the primordial building blocks for the subsequent galaxy formation and growth. As Figure 1.1.2 shows, the Universe at this epoch ($z > 8$) was mostly neutral, with the ionization fraction increasing up to 50% at $z \sim 7$, and becoming predominantly ionized at $z < 6$ (e.g., Fan et al., 2006a; Robertson et al., 2015; Ota et al., 2017; Greig and Mesinger, 2017).

The evolution of the cosmic neutral fraction remains a very challenging question, and one of the main candidates to explain this evolution is the stellar activity of the first galaxies (Fan et al., 2006b). Detecting and studying these early systems, and their role in the cosmic reionization of the Universe, represents a current major observational challenge.

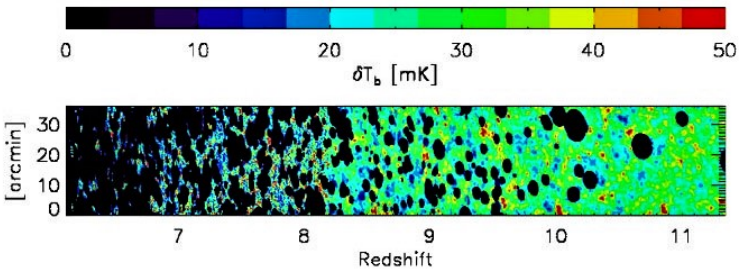

Figure 1.1.2: Cosmic reionization process as a function of z. Simulation of the [HI] 21 cm emission considering radiative transference. Figure adapted from Thomas et al. (2009).

The discovery of massive galaxies ($> 10^8$ $M_\odot$) in the first $\sim 1-2$ Gyr of the Universe (e.g., Oesch et al., 2016; Glazebrook et al., 2017; Strandet et al., 2017; Marrone et al., 2018; Bañados et al., 2018; Jiang et al., 2021) allows us to ask again about how galaxies began to form large numbers of stars in the first stages of the Universe. The study of interstellar medium at very high-z using fine-structure lines such as the [CII] 158 μm and/or [OIII] 88 μm transitions provides a relevant measure of the star formation activity and ISM properties in early epoch galaxies (e.g., Bouwens et al., 2021).

1.1.3 How to study very high-z galaxies?

To date, the study of high-z galaxies is unfortunately limited to a little amount of tracers. One of the most powerful tools to study high-z galaxies is the [CII] 158 μm transition, that probes the ISM of the galaxy. Another important tracer of high-z systems is the Lyα emission line from young and massive stars. I will discuss in more detail about these two tracers in Chapter 2.

1.2 Galaxias a muy alto redshift

Este proyecto se enfoca en el estudio de las propiedades del medio interestelar y el ambiente de una galaxia típica cerca de la época de reionización, es decir, a redshift (z) entre 6 y 8. Por esta razón, es necesario partir aclarando algunos conceptos claves en el estudio de sistemas a muy alto redshift.

1.2.1 ¿Qué es una galaxia a muy alto redshift?

No hay una respuesta simple para esta pregunta, en parte porque el punto de vista teórico y observacional tienen diferentes definiciones, y tambiién porque los desarrollos tecnológicos cambian la definición a medida que detectamos sistemas más lejanos.

Desde una perspectiva observacional, una simple definición para una galaxia a muy alto redshift corresponde a la galaxia al más alto redshift actualmente observada. Obviamente esta definición cambia con el tiempo y va de la mano con los desarrollos técnicos y tecnológicos. Una definición un poco más elavorada es una galaxia con una metalicidad (Z) muy cercana a cero (o cero), pero esto podría ser engañoso puesto que incluso las primeras galaxias podrían haber sido enriquecidas por metales por super novas (SNe) desencadenadas por las primeras estrellas (ver Bromm and Yoshida (2011)).

Por simplicidad, en este trabajo voy a considerar como galaxia a muy alto redshift todas las fuentes a $z > 6$ detectadas hasta ahora. Esta no es una mala suposición, aún más si consideramos el modelo cosmológico ΛCDM, donde las estructuras se forman de manera jerárquica a través de la fusión de halos más pequeños de materia oscura. La Figura 1.1.1 muestra una representación de la formación de las primeras galaxias, donde las primeras galaxias a $z \sim 10$ fueron formadas a través del colapso de mini halos de materia oscura a $z \sim 20$.

1.2.2 ¿Por qué estudiar galaxias a muy alto redhsift?

Se piensa que las primeras galaxias se formaron dentro de los primeros $\sim 200 - 300$ Myr de vida del Universo (e.g., Bromm and Yoshida, 2011; Wise et al., 2011). Estos sitemas son reconocidos como los impulsores claves de la evolución cósmica temprana, y representan los bloques de construcción primordiales en la subsiguiente

formación de galaxias y su crecimiento. Como muestra la Figura 1.1.2, en esta época ($z > 8$) el Universo estaba mayormente neutral, con la fracción ionizada aumentando hasta un 50% a $z \sim 7$, y luego volviendo mayormente ionizado a $z < 6$ (e.g., Fan et al., 2006a; Robertson et al., 2015; Ota et al., 2017; Greig and Mesinger, 2017).

La evolución de la fracción cósmica neutral se mantiene como una pregunta muy desafiente, y uno de los principales candidatos para explicar esta evolución es la actividad estelar de las primeras galaxias (Fan et al., 2006b). Detectar y estudiar estos sistemas tempranos, y su rol en la reionización cósmica del Universo, representa un gran desafió en las observaciones actuales.

El descubrimiento de galaxias masivas ($> 10^8$ $M_\odot$) en los primeros $\sim 1 - 2$ Gyr del Universo (e.g., Oesch et al., 2016; Glazebrook et al., 2017; Strandet et al., 2017; Marrone et al., 2018; Bañados et al., 2018; Jiang et al., 2021) nos permite preguntarnos nuevamente sobre cómo las galaxias comenzaron a formar grandes numeros de estrellas en las primeras etapas del Universo. El estudio del medio interestelar a muy alto z usando las lineas de estructura fina como la transición [CII] 158 μm y/o [OIII] 88 μm proporciona una medida relevante de la actividad de formación estelar y las propiedades del ISM en galaxias de épocas tempranas (e.g., Bouwens et al., 2021).

1.2.3 ¿Cómo estudiar galaxias a muy alto redshift?

Hasta ahora, el estudio de galaxias a alto z está desafortunadamente limitado a un pequeño grupo de trazadores. Una de las herramientas más útiles para estudiar galaxias a alto z es la transición [CII] 158 μm, la cual sondea el ISM de la galaxia. Otro trazador importante es la emisión de Lyα proveniente de estrellas jóvenes y masivas. Voy a discutir en mayor detalle estos dos trazadores en el Capítulo 2.

Chapter 2

Theoretical Framework

2.1 Lyα emission

An important tracer of high-z systems is the Lyα line. This line is produced when an electron in the $2p$ state decays to the ground state. Two scenarios can produce the Lyα emission. The first one is by collisional excitation, where a hydrogen atom collides with a free electron. The collision can leave the atom in an excited state, depending on the kinetic energy of the free electron. The second case is the recombination between protons and electrons. Radiative cascades to the ground state can then produce a Lyα photon (Dijkstra, 2017).

2.1.1 Lyα observations in high-z galaxies

The Lyα line at 1215 Å (rest-frame) can be observed in high-z galaxies using ground-based telescopes in the near-IR wavelength range. Lyα emission comes from the radiation emitted by young and massive stars, but does not suffer any absorption by the gas surrounding the emitter stars.

One of the most useful technique to identify high-z candidates is the Lyman break drop-out. Thanks to this technique we have identified hundreds of $z > 6.5$ candidates systems (e.g., Steidel et al., 1996; Giavalisco, 2002). This technique is based on the large break in the continuum flux from an object that occurs at the 912 Å Lyman limit from neutral hydrogen absorption in the line-of-sight. Taking multi-band images of a field that contains high-z galaxies, this technique can be used to identify those objects that have very red colors as a result of the

redshifted Lyman limit falling between any two filters (Illingworth, 1999).

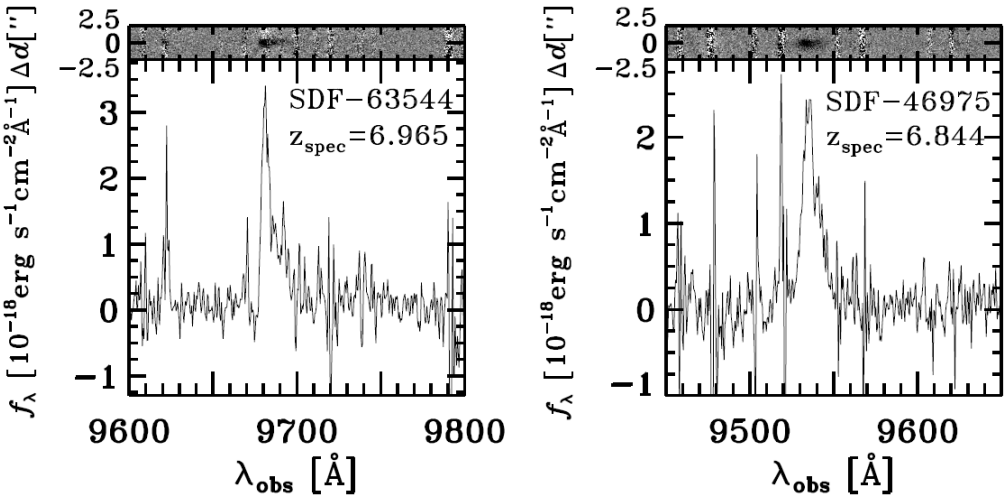

Figure 2.1.1: Prominent two Lyα detections of SDF-63544 (left) and SDF-46975 (right). The top panels show the composite two-dimensional spectra of both galaxies. Figure adapted from Ono et al. (2011).

Ono et al. (2011) performed spectroscopic observations of z-dropout candidates discovered in Ouchi et al. (2009) using the DEep Imaging Multi-Object Spectrograph (DEIMOS; Faber et al., 2003) at the 10 m Keck II telescope. Figure 2.1.1 shows two examples of the Lyα detections of these candidates. In the case of the galaxy SDF-63544 (left) the Lyα line is detected at 9683 Å with a signal to noise (S/N) of ~ 13, and for SDF-46975 (right) the Lyα detection is at 9536 Å with a S/N of ~ 14.

Similar results were reported in several works in the last years (e.g., Ning et al., 2021; Endsley and Stark, 2021). Figure 2.1.2 shows a sample of 36 selected Lyα emitters galaxies between $6.492 < z < 6.625$ detected in the Lyα line. The large number of Lyα detections has allow us to study the epoch of cosmic reoinization, where the neutral hydrogen in the intergalactic medium (IGM) was ionized by the UV radiation from the first stellar objects (e.g., Jiang et al., 2013).

However, because of the nature of the Lyα emission, we receive only the radiation from young stars that is not obscured or absorbed by atomic hydrogen and/or dust. If we want to study the different phases of ISM in very high-z galaxies, we need another tracer that gives us information about the star formation, morphology, and kinematics, such as the [CII] 158 μm transition.

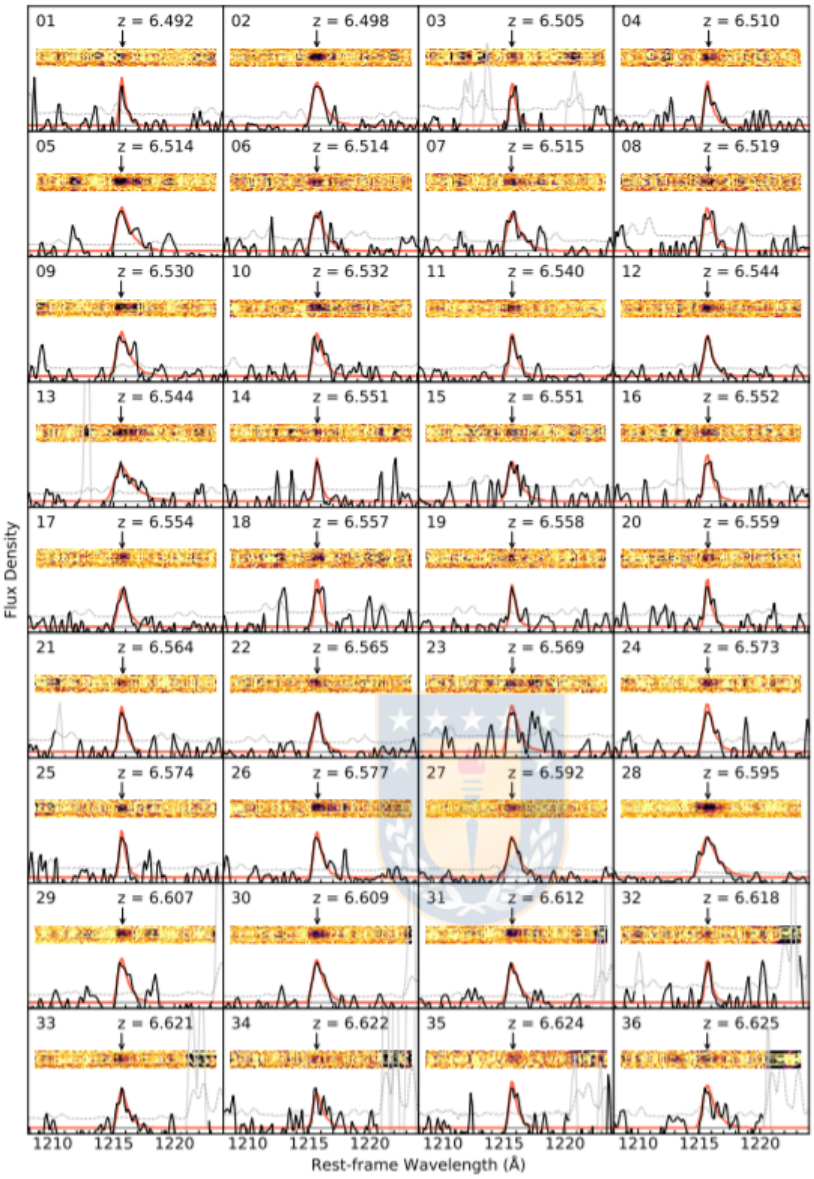

Figure 2.1.2: Lyα line emission in a sample of 36 galaxies at $z > 6$ detected using the Lyman break drop-out technique. Figure adapted from Ning et al. (2021)

2.2 [CII] 158 μm transition

The [CII] 158 μm transition is one of the main cooling channels of the ISM (e.g., Wolfire et al., 2003). This line is produced by collisional excitation with electrons, neutral hydrogen (HI) and molecular hydrogen (H_2), with relatively low critical densities of 44, 3×10^3 and 6×10^3 cm^{-3}, respectively (Goldsmith et al., 2012). Due to the relatively low ionization potential of the carbon atom (11.2 eV), the [CII] 158 μm transition can be used as a tracer of molecular, atomic and ionized gas.

Given that due to technical limitations the HI 21 cm line is currently unoservable at $z > 1$, the [CII] line represents an excellent alternative to study the extended disk, kinematics, and halo emission of high-z systems (e.g., Fujimoto et al., 2020; Herrera-Camus et al., 2021).

2.2.1 [CII] 158 μm - FIR ratio

Figure 2.2.1 shows the ratio between the [CII] and FIR continuum luminosity ($L_{\rm FIR}$) as a function of the FIR luminosity. For all types of sources (included galaxies at $z > 1$) the [CII]/FIR ratio remains roughly constant ($L_{\rm FIR} < 10^{11}$ L$_\odot$) with values that range between $10^{-3} - 10^{-2}$. For galaxies with higher L$_{\rm FIR}$ (L$_{\rm FIR} > 10^{11}$ L$_\odot$), also known as luminous infrared galaxies (LIRGs), the [CII]/FIR ratio drops, although accompanied by an increase in the scatter of a factor of ~ 2 (Herrera-Camus et al., 2018). Independent of the observed [CII] deficit at high $L_{\rm FIR}$, the [CII] 158 μm transition is one of the brightest lines in star-forming galaxies. In addition, the [CII] line remains bright in metal-poor environments, such as those we expect to find in high-z galaxies (e.g., Israel and Maloney, 2011; Cormier, 2014; Cigan et al., 2015).

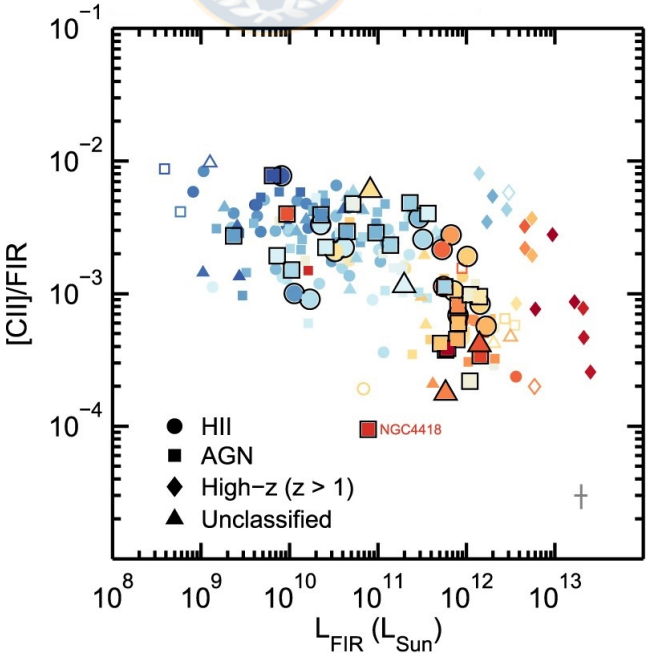

Figure 2.2.1: [CII] 158 mμ line to FIR continuum rate for different types of galaxies and also for high-z systems ($z > 1$) against FIR luminosity. Figure adapted from (Herrera-Camus et al., 2018)

2.2.2 [CII] 158 μm at $z > 6$

Until just recently, the study of the most massive early-type galaxies ($z > 6$) was limited to the sensitive near-IR observations from the *Hubble Space Telescope* (HST), i.e., young and massive stars not obscured by dust; mid-IR observations from *Spitzer*, i.e., probing line emission and stellar population age through the features like Balmer break; and rest frame UV spectroscopy from ground telescopes (e.g., *Subaru Telescope*) observations, i.e., Lyα and some high ionized UV lines detections from very young stellar populations (e.g., Ono et al., 2011; Zitrin et al., 2015; Stark et al., 2017).

Over the last decade this scenario has significantly changed. Thanks to the improved capabilities of the *NOrthern Extended Millimeter Array* (NOEMA) and *Atacama Large Millimeter/sub-millimeter Array* (ALMA), we now can characterize the physical properties of the ISM in star-forming galaxies at very high-z through FIR fine-structure lines such as the [CII] 158 μm and [OIII] 88 μm transitions.

Until just recently, [CII] observations of massive $z > 6$ galaxies were restricted to those with strong Lyα emission (e.g., Venemans et al., 2019, 2020). However, this scenario is changing. Several ALMA large programs (e.g., Smit, 2018; Schouws et al., 2021) have shown that scanning Lyman break selected, UV-bright galaxies (not necessarily bright in Lyα emission) for prominent ISM-cooling lines can be a very efficient way to identify luminous galaxies in the $z > 6$ Universe. Based on this strategy, Bouwens et al. (2021) targeted 40 bright, star-forming galaxies as part of the Reionization Era Bright Emission Line Survey (REBELS), a cycle-7 ALMA large program. Figure 2.2.2 shows the detection of the [CII] 158 μm transition in the $z > 6$ star-forming galaxies from REBELS.

2.2.3 Star formation rate - [CII] luminosity relation

Under the assumption of an ISM in thermal equilibrium, and considering that the [CII] 158 μm transition is one of its main cooling channels (e.g., Wolfire et al., 2003), a tight relation is expected between the cooling via the [CII] line emission, and the principal heating source, i.e., the star formation activity. This relation has been observed in nearby, star-forming galaxies and high-z, main-sequence systems (e.g., De Looze et al., 2014a; Herrera-Camus et al., 2015; Herrera-Camus et al., 2018; Schaerer et al., 2020).

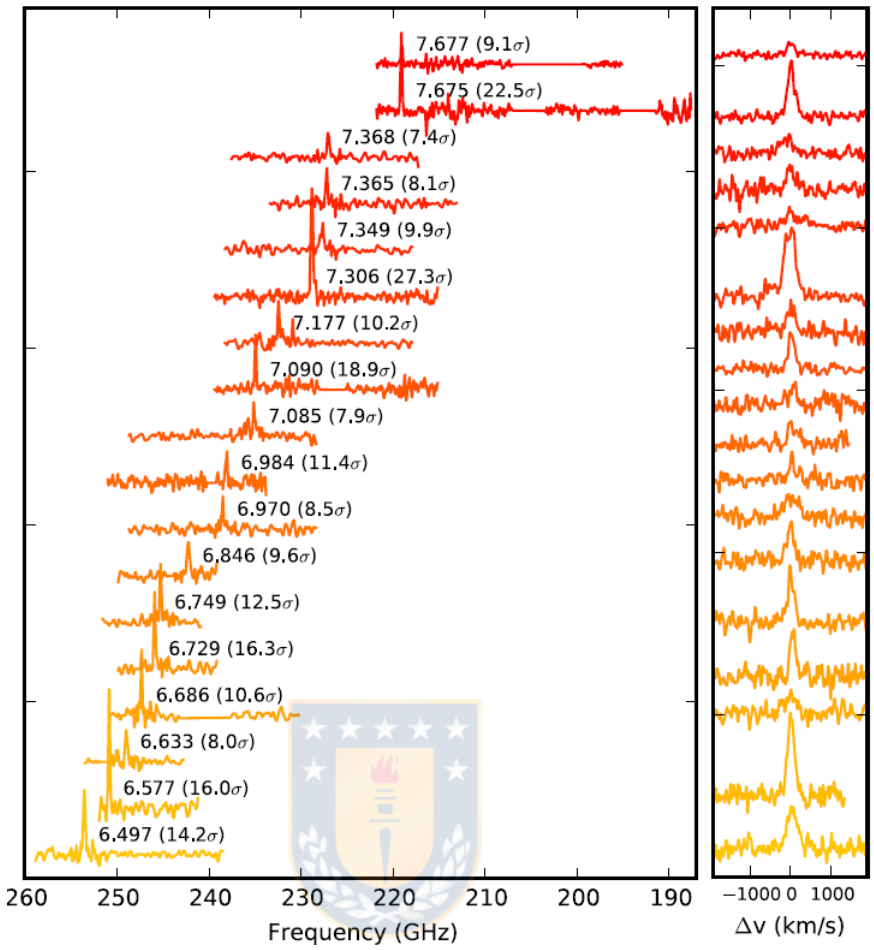

Figure 2.2.2: Highest significance ($\geq 7\sigma$) levels of detection in the REBELS large program. Figure adapted from Bouwens et al. (2021).

Figure 2.2.3 shows the [CII] surface brightness - star formation rate (SFR) surface density relation for spatially resolved regions ($\sim$ 1 kpc) from 46 galaxies from the KINGFISH sample (Herrera-Camus et al., 2015). The different panels show different methods to estimate the SFR value for each galaxy. For all panels in the bottom-right corner is the value of the slope (m), the value of the y-axis at $x = 40$ (N) and the standard deviation (σ) in dex. Using the OLS linear bisector method (Isobe et al., 1990) to estimate the best linear fit to the data, Herrera-Camus et al. (2015) find that the $\Sigma_{\rm SFR}$ and $\Sigma_{\rm [CII]}$ yields the following relationship:

$$\Sigma_{\rm SFR}\ ({\rm M}_\odot\ {\rm yr}^{-1}{\rm kpc}^{-2}) = 3.79 \times 10^{-47} \times (\Sigma_{\rm [CII]}\ [{\rm erg\ s}^{-1}{\rm kpc}^{-2}])^{1.13}$$

The great utility of the [CII] 158 μm transition, not only to detect high-z systems, but also to estimate properties such as SFR, together with the

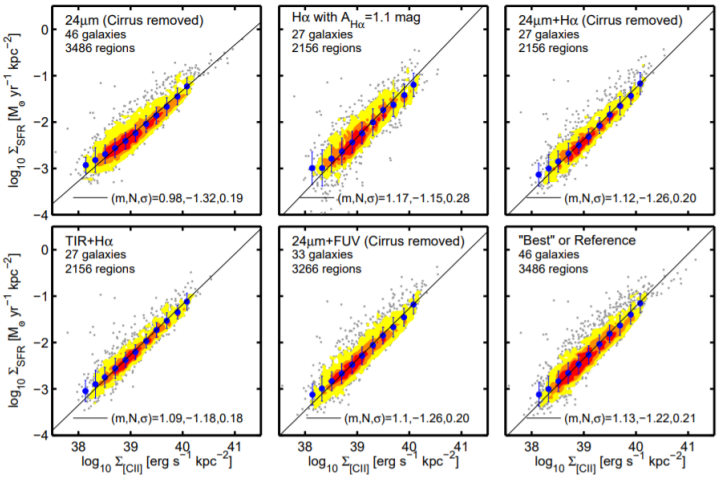

Figure 2.2.3: $\Sigma_{\rm SFR}$ and $\Sigma_{\rm [CII]}$ scaling relation using different SFR tracers. In all panels m, N and σ indicate the slope of the relation, y-axis value at $x = 40$ and the standard deviation in dex, respectively. Figure adapted from Herrera-Camus et al. (2015)

improving capabilities of the current interferometers, have opened the possibility to characterize the ISM and star formation processes in galaxies at $z > 6$, which is fundamental to understand the early phases of galaxy formation and evolution (e.g., Dayal and Ferrara, 2018).

2.3 [CII] 158 μm - Lyα offsets

The [CII] 158 μm and Lyα transitions trace different structures, dust content, and ISM phases of the galaxy. Therefore, potential differences between the line systemic velocities and profile shapes give us information about the ISM properties, and the environment surrounding the galaxy.

2.3.1 Lyα - [CII] spatial offset

Multi-wavelength observations of star-forming galaxies at $z > 6$ have reported spatial offsets between tracers of the dust/cold gas (e.g., [CII], dust continuum), and tracers of the ionized gas (e.g., Lyα, [OIII]). For example, Carniani et al. (2018) observed BDF-3299, a star-forming galaxy at $z = 7.1$, using UV continuum, Lyα, [CII] and [OIII] 88 μm emission. Figure 2.3.1 shows the large spatial offset observed between the [CII] (red contours), [OIII] 88 μm (blue contours), and the rest-frame UV emission from HST (background). The observed spatial offset is

not due to astrometric problems between the different datasets.

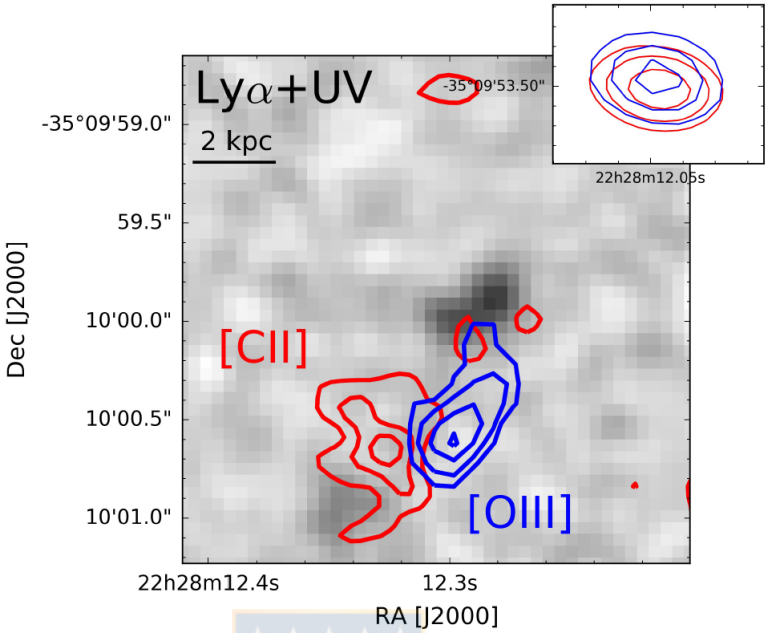

Figure 2.3.1: Spatial offset between Lyα + UV (grey scale), [CII] (red contours) and [OIII] emission. Figure adapted from Carniani et al. (2018)

Theoretically, this spatial offset can be explained in terms of the strong UV emission in the main galaxy and gas accretion process from the CGM. Figure 2.3.2 shows the model of primeval galaxies developed by Vallini et al. (2013) tailored to a galaxy at $z = 7.1$ (Maiolino et al., 2015). In this model, the gas in the main galaxy is completely ionized, while molecular gas are not present due to the strong stellar feedback. Black points indicates the spatial distribution of young massive stars, i.e., the stars that we observe through UV continuum emission. In color is shown the warm ionized gas distribution, which can be observe via the Lyα line. Contours indicate [CII] 158 μm emission coming from neutral and middle ionized gas.

2.3.2 Lyα - [CII] velocity offset

Due to the radiative transfer processes that affect the Lyα photons, the systemic velocity of the Lyα line does not necessarily match the systemic redshift ($z_{\rm sys}$) of the galaxy. In that sense, optically-thin lines such as [CII], [OIII] or Hα, which are not affected by any radiative transference process, can provide the real redshift of the source.

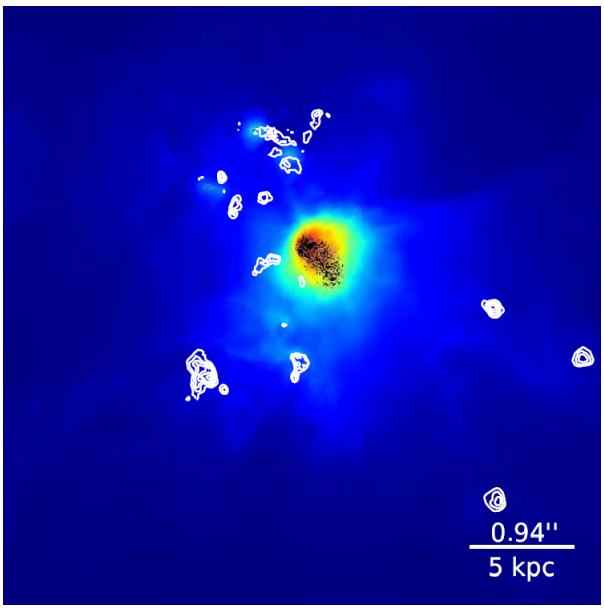

Figure 2.3.2: Simulation of a primeval galaxy at $z \sim 7$. Figure adapted from Maiolino et al. (2015).

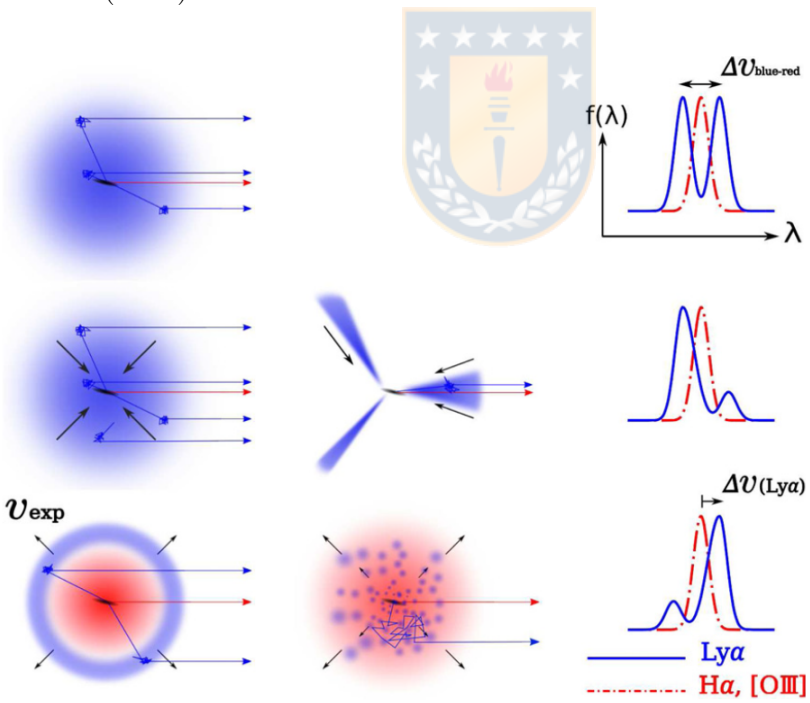

Figure 2.3.3: Schematic representation of the expected Lyα and non-resonant photons (e.g., [CII] or [OIII]) if the gas in the blobs surrounding the galaxy is static (top), inflowing (middle) and outflowing (bottom). The solid blue and red dotted line represent the Lyα emission and non-resonant line, respectively. Figure adapted from Yang et al. (2014).

The difference between the velocity of the Lyα and non-resonant lines, $\Delta v_{\text{Ly}\alpha}$,

provides a valuable probe of the ISM and also the surrounding IGM (Hashimoto et al., 2019). $\Delta v_{\mathrm{Ly}\alpha}$ has been investigated in hundreds of galaxies at $z \approx 2-3$ based on observations of the Lyα and Hα (or [OIII]) lines (e.g., Hashimoto et al., 2013). At this redshift, galaxies have $\Delta v_{\mathrm{Ly}\alpha}$ ranging from 100 to 1000 km s^{-1}, with mean value of 300 km s^{-1} (e.g., Erb et al., 2014). At $z > 6$, galaxies tend to have $\Delta v_{\mathrm{Ly}\alpha}$ that range between $100-500$ km s^{-1} (e.g., Carniani et al., 2018; Bouwens et al., 2021). To date, the highest $\Delta v_{Ly\alpha}$ value reported is 772 km s^{-1} in the star forming galaxy B14-65666 at $z = 7.15$ (Hashimoto et al., 2019).

The physical reasons behind the observed $\Delta v_{\mathrm{Ly}\alpha}$ are explored in the context of a galaxy lying in a Lyα halo by Yang et al. (2014). For this configuration, Figure 2.3.3 illustrate three different possible scenarios. The first (top) is a static cloud, where the Lyα photons in the Doppler wings escape in random scatterings. The observed spectral profile will be double peaked in the Lyα emission, centered at the systemic redshift of the galaxy. In this case, both z_{sys} and $z_{\mathrm{Ly}\alpha}$ are the same. The middle panel shows the infalling gas scenario. In this case, Lyα photons on the red side of the double-peaked profile see higher optical depth due to the line-of-sight infalling gas, and the red peak is depressed, which implies a Lyα spectral profile blueshifted with respect to z_{sys}. The bottom panel shows the outflowing gas scenario. Here, unlike the previous case, the blue peak is depressed due to the scatter suffered for the outflowing gas, which contributes to the red peak of the Lyα line. This implies a $z_{\mathrm{Ly}\alpha}$ redshifted relative to the z_{sys} of the source. For the outflowing scenario, a first order approximation to relate the expansion velocity of the blob or the outflow velocity (v_{out}) with $\Delta v_{\mathrm{Ly}\alpha}$ is (e.g., Verhamme et al., 2006):

$$v_{\mathrm{out}} = \frac{\Delta v_{\mathrm{Ly}\alpha}}{2}. \tag{2.3.1}$$

Figure 2.3.4 shows a compilation of the Lyα velocity offset observed in a sample of $z \gtrsim 6$ star-forming galaxies (Hashimoto et al., 2019). The left panel shows the anti-correlation observed between $\Delta v_{\mathrm{Ly}\alpha}$ and Lyα equivalent width (EW$_0$(Lyα)). This anti-correlation could be explained in terms of a the presence of a large hydrogen column density that decreases EW$_0$(Lyα) (due to a higher dust content along the line of sight) and increase $\Delta v_{\mathrm{Ly}\alpha}$ due to resonant scattering. The middle and right panels show the correlation of $\Delta v_{\mathrm{Ly}\alpha}$ with absolute UV magnitude and

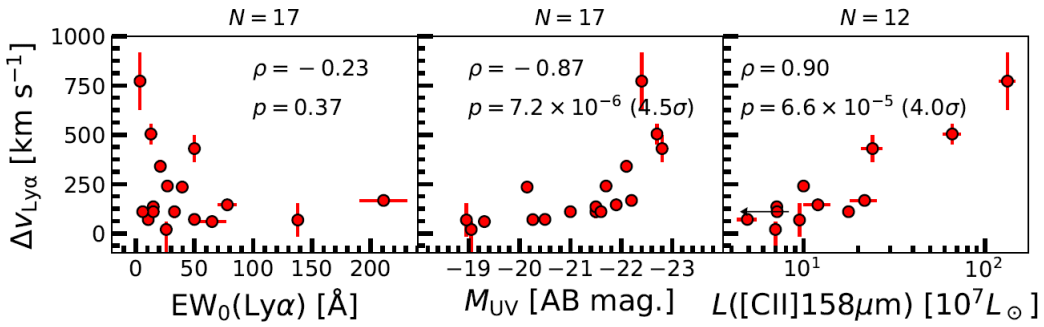

Figure 2.3.4: Compilation by Hashimoto et al. (2019) of $\Delta v_{\mathrm{Ly}\alpha}$ as a function of Lyα equivalent width (left), absolute UV magnitude (center), and [CII] luminosity for high-z galaxies ($z \sim 6-8$). In all three panels N, ρ and p indicates the number of individual data points, the Spearman rank correlation coefficient for each relation and the probability satisfying the null hypothesis, respectively. Figure adapted from Hashimoto et al. (2019)

[CII] luminosity, respectively. Both trends can be interpreted as an increase in the expanding gas velocity due to starburst driven outflow, hence the UV luminosity. These correlations and interpretations will be discuss in more detail in Section **??**.

For this work we adopt the following cosmological parameters: $H_0 = 67.4$ km s^{-1} Mpc^{-1}, $\Omega_M = 0.315$ and $\Omega_\Lambda = 0.685$ (Planck Collaboration et al., 2020). For a source at $z = 7.21$, this results in a physical scale of 5.24 kpc/$''$.

Chapter 3

Methodology and Results

3.1 Observations and data reduction

3.1.1 Target

In this project we focus on the combined analysis of Lyα and [CII] line emission in GN-108036, a star-forming galaxy at $z = 7.213$. The redshift of GN-108036 is based on the detection of the Lyα line from deep Keck/DEIMOS spectroscopy (Ono et al., 2011). This makes GN-108036 one of the most distant sources known in the Northern Hemisphere (dec. +62:08:07). Figure 3.1.1 shows the Lyα detection of the galaxy by Ono et al. (2011). The main argument in favor of the observed line being Lyα is its morphology and the clear asymmetry of the line. In addition, if the detected line were Hβ or [OIII] at $z \sim 0.9 - 1.0$, additional lines should be detected. In the case of Hβ, the [OIII] should fall at 10284 Å, and in the case of [OIII], the Hβ would be seen at 9674 Å. In both hypothetical cases the corresponding non-detection of additional lines support the idea that is a Lyα detection at $z = 7.213$. In the case of the asymmetry, Ono et al. (2011) used the weighted skewness parameter (S_w), that is defined as the product of the skewness (the third moment of flux distribution) and the width of the line. In general Lyα emission lines in high-z galaxies have large positive S_w parameter, while other possible lines, e.g., Hα, Hβ, and [OIII] are symmetric with S_w values very close to zero. The S_w value is estimated to be $S_w = 4.1 \pm 0.7$ Å for GN-108036, which means that the detected line has an asymmetric profile with a sharp decline on the blue side and a long tail on the red side, that as we saw in Section 2.2, is

typical in very high-z galaxies.

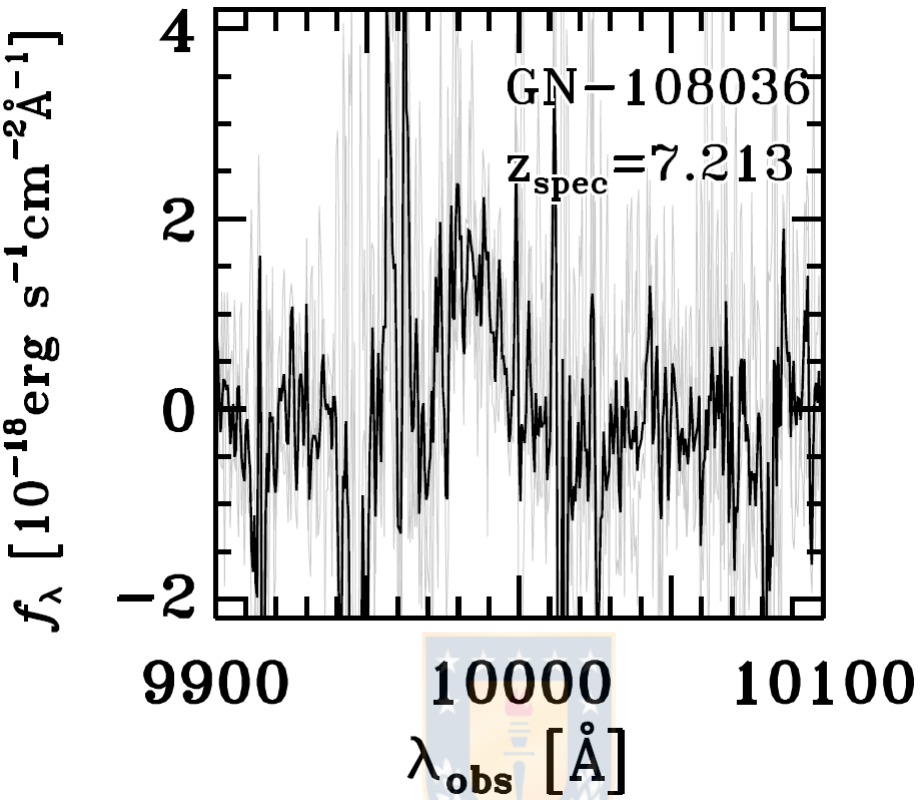

Figure 3.1.1: Lyα spectral profile of GN-108036 obtained using the DEep ImagingMulti-Object Spectrograph at the Nasmyth focus of the 10 meters Keck II telescope. Figure adapted from Ono et al. (2011).

The stellar mass of GN-108036 is $M_\star = 10^{8.76}\ M_\odot$, and its star formation rate (SFR) is in the 29 to 100 $M_\odot$ yr^{-1} range based on calculations using the rest-frame UV continuum and stellar population synthesis models, respectively (Ono et al., 2011). Figure 3.1.2 shows the HST (F140W) map of the source in grey scale. The HST map shown corresponds to an area of $\sim 7.5'' \times 7.5''$ where the black circle indicates the position of the galaxy.

3.1.2 NOEMA interferometer

In our work we use observations of the ionized carbon [CII] 157.74 μm transition by the Northern Extended Millimeter Array (NOEMA) to detect and characterize the galaxy and its environment, and compare it to the Lyα line emission.

NOEMA is one of the most powerful millimeter interferometers. This array of radiotelescopes developed by Institut de Radioastronomie Millimétrique (IRAM)

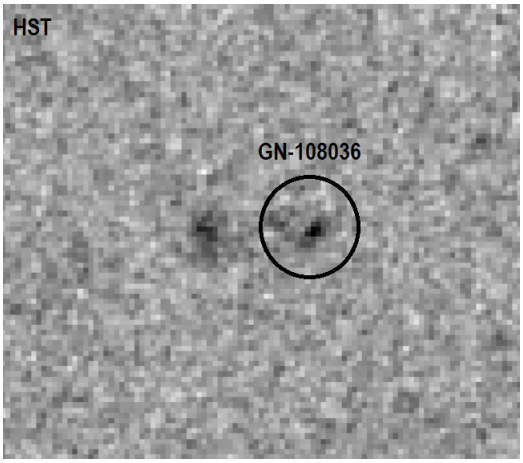

Figure 3.1.2: HST rest-frame UV map of the field of GN-108036. Black circle indicates the position of the galaxy.

is located in the French Alps at an elevation of 2550 meters. Currently has 12 antennas, each one of them of 15 meters in diameter. The array has two tracks, extending on the north-south and east-west direction, with a maximum separation of 760 meters in E-W and 230 meters in N-S. In this extended configuration the array reaches a resolution of 0.5 arcsecs at an observing wavelength of 1.3 mm (230 GHz).

Figure 3.1.3: Seven antennas of the NOEMA observatory in the French Alps at 2550 meters above sea level. Credits: IRAM (www.iram-institute.org)

Due to the redshift of our source, the [CII] transition is redshifted to $\nu_{\mathrm{[CII],obs}} =$

231.5 GHz, which falls into NOEMA Band 3. Figure 3.1.4 shows the Band 3 of NOEMA, indicating the frequency where we expect to detect the [CII] 158 μm transition (magenta and blue arrow).

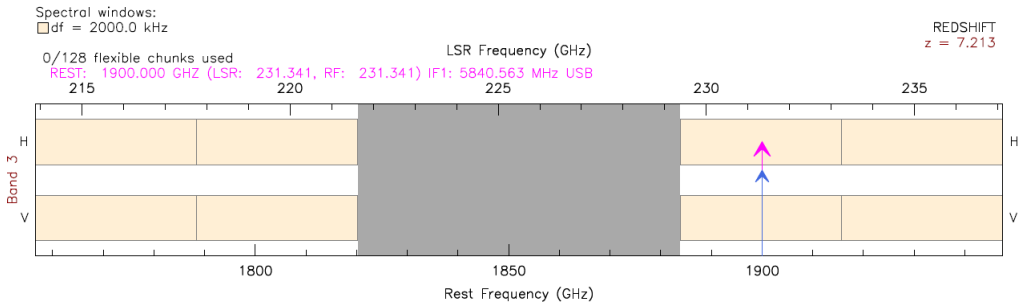

Figure 3.1.4: Instrumental tuning of NOEMA Band 3.

3.1.3 NOEMA observations

GN-108036 was first observed in March 2019 using the most compact array configuration (D) for an on-source time of 3.2 hrs. The second set of observations was taken on March 2020 using array configuration C for an on-source time of 3.7 hrs. We reduced and combined both data sets using the `CLIC` and `MAPPING` software by IRAM.[1] For the imaging of the [CII] cube and the dust continuum map we use natural weighting to maximize the sensitivity. The resulting synthesized beam for the D, C, and combined C+D data was $\theta = 2.1'' \times 1.5''$, $\theta = 1.2'' \times 0.9''$, and $\theta = 1.4'' \times 1.1''$, respectively. The rms noise for the D, C, and combined C+D line cubes is 0.46, 0.35, and 0.35 mJy beam^{-1} in 25 km s^{-1} channels, respectively.

In all three data sets the spectral resolution is 25 km s^{-1} with 386 channels covering a velocity range of $\sim$ 10000 km s^{-1} from ~ -7000 km s^{-1} to $\sim +2600$ km s^{-1}.

3.1.3.1 Dust continuum

We created a continuum map using using the sidebands of the C+D data where we do not expect line emission from the source. The root mean square (rms) noise in the continuum map is 13 μJy beam^{-1}. Figure 3.1.5 shows the NOEMA dust continuum map at 218 GHz around GN-108036. Unfortunately, we did not detect the source.

[1] CLIC and MAPPING are part of the GILDAS package (Guilloteau and Lucas, 2000): http://www.iram.fr/IRAMFR/GILDAS

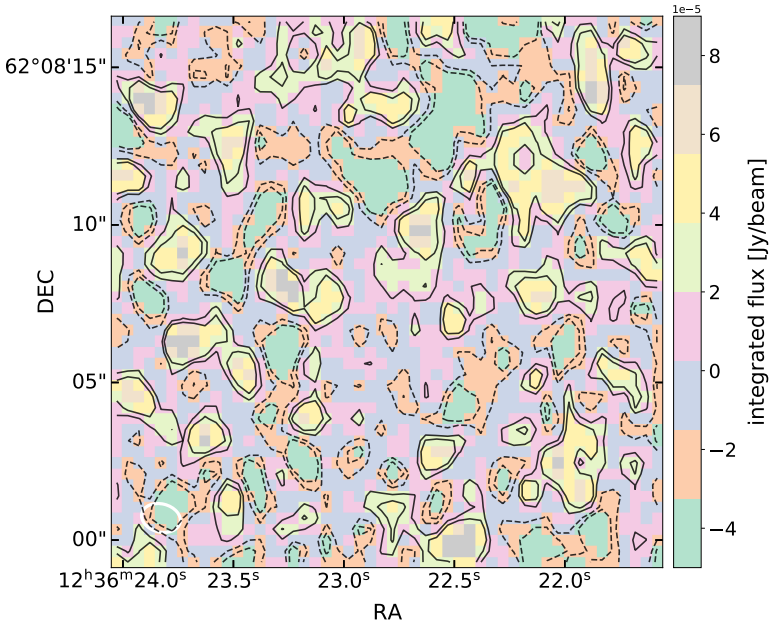

Figure 3.1.5: NOEMA dust continuum map of GN-108036 using the lower side band (LSB, $\nu_{\rm restfreq} = 218$ GHz) of the spectral window. Black solid contours are at levels of 1 and 2σ ($\sigma = 13$ μJy beam^{-1}). Dashed contours trace negative levels at -1 and -2σ.

Assuming a characteristic dust temperature for a $z \sim 6-7$ galaxy of $T_{\rm dust} = 45$ K (e.g., Schreiber et al., 2018; Faisst et al., 2020), and a dust emissivity index of $\beta = 1.5$ we can estimate the dust mass upper limit of the galaxy using the following relation (e.g., Ota et al., 2014):

$$M_{\rm dust} = \frac{F_{\rm obs} D_{\rm L}^2}{(1+z)\kappa(\nu_{\rm rest})[B_\nu(T_{\rm dust}(z)) - B_\nu(T_{\rm CMB}(z))]} \quad , \tag{3.1.1}$$

where $F_{\rm obs}$ is the observed flux, $D_{\rm L}$ is the luminosity distance of the source in Mpc, $\kappa(\nu_{\rm rest}) = 0.77(850\mu{\rm m}/\lambda_{\rm rest})^\beta$ cm^2 g^{-1} (Dunne et al., 2000) is the dust mass absorption coefficient (with $\lambda_{\rm rest} = 158\mu$m), and $B_\nu(T_{\rm dust})$ is the Planck function at a rest frequency $\nu_{\rm rest}$ and a dust temperature $T_{\rm dust}$.

The expected non-detection indicates a 3σ dust mass upper limit of $M_{\rm dust} < 9.5 \times 10^6$ $M_\odot$. The low dust content in GN-108036 is consistent with that observed in other $z \approx 7$ systems (e.g., Maiolino et al., 2015).

3.1.4 Tentative detection of the [CII] 158 μm transition in GN-108036

We searched for [CII] line emission by systematically placing apertures of the beam size across the cubes separated by a distance of a quarter of a beam size. For this we use the `Spectral Cube` package of `Python 3.8.3`.

We tentatively detected two sources with an integrated signal-to-noise (S/N) of ≈ 3 in two regions of the cube: 1) in the center, and slightly offset from the spatial position of the detection of GN-108036 in the HST rest-frame UV and Lyα data, and 2) about $\sim$30 kpc east from the HST detection of GN-108036.

The top-left panel of Figure 3.1.6 shows the CII] spectrum of the potential detection of GN-108036 extracted from the compact array NOEMA data. From a single Gaussian fit we find that the line is centered at -982 ± 13 km s^{-1} with respect to the detection of the Lyα line (Ono et al., 2011). We discuss more about this large velocity offset in Chapter 4. The integrated CII] flux is 0.21$\pm$0.07 Jy km s^{-1}, which corresponds to a tentative detection of the source with a S/N of ≈ 3. The signal is present in the $\sim 2\times$ higher angular resolution data set at the same velocity range, but with lower significance. This could be the result of the CII] line emission in GN-108036 to be significantly more extended than 1" ($\sim$ 5 kpc), as it has been observed in other $z \sim 6-7$ star-forming galaxies (e.g., Carniani et al., 2020).

Table 3.1.1: [CII] 158 μm fluxes and parameters from the Gaussian fit to the tentative detections of GN-108036 and its companion

Source	SFR $[M_\odot$ yr$^{-1}]$	$z_{\mathrm{Ly}\alpha}$	$z_{[\mathrm{CII}]}$	Central velocity [km s^{-1}]	FWHM [km s^{-1}]	Integrated Flux [Jy km s^{-1}]	Luminosity $10^8 L_\odot$
GN-108036	$\sim 30-100$	7.213	7.180	-982.2 ± 12.7	102.7 ± 29.9	0.21 ± 0.07	2.7
Companion	–	–	7.188	-910.1 ± 57.2	503.5 ± 134.7	0.47 ± 0.15	6.0

We constructed a [CII] integrated intensity map (or moment 0) integrating the [CII] line emission around the potential detection of the line centered at the velocity of -982 km s^{-1}. Figure A0.2 in the Appendix shows the [CII] moment 0 map, and the right panel of Figure 3.1.6 shows the [CII] integrated intensity contours (at significance levels of 2.5, 3, 4 and 5σ) overplotted on the HST/WFC3 map of the field. The dotted black circle in the center indicates the position of GN-108036 as detected in the rest-frame UV and Lyα emission (Ono et al., 2011). The peak of the integrated [CII] line emission is offset with respect to the peak of

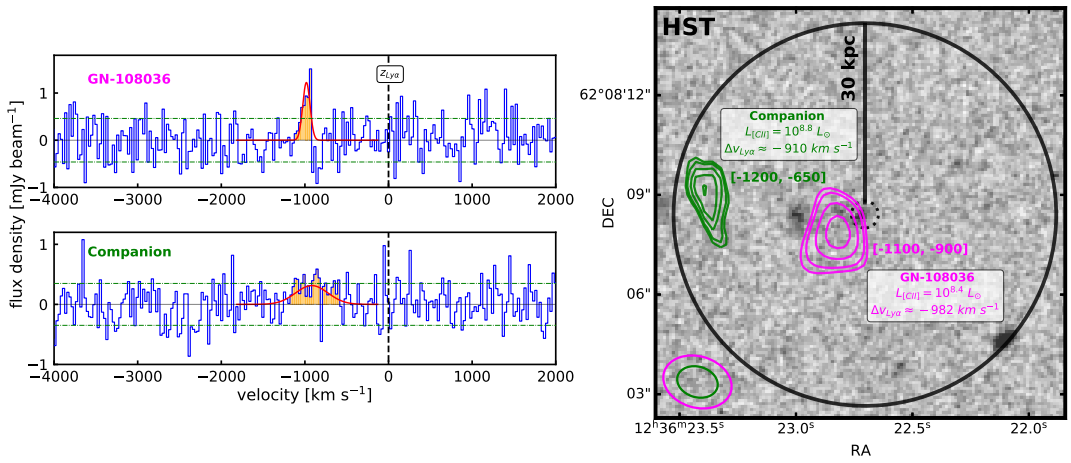

Figure 3.1.6: *Left:* [CII] line spectrum of GN-108036 (top) and a potential companion located $\sim$ 30 kpc east (bottom). The zero velocity is set using the redshift from the detection of the Lyα line (black dashed vertical line Ono et al., 2011). The best 1D Gaussian fits to the tentative detections are shown in red. *Right:* HST rest-frame UV map of the field of GN-108036. The black dotted circle indicates the position of the HST rest-frame UV emission from GN-108036, and the black solid circle around the center has a radius of 30 kpc. The integrated intensity contours of the CII] line emission (2.5, 3, 4 and 5σ levels) are shown in magenta for the potential detection of GN-108036, and green for the potential companion.

the rest-frame UV and Lyα emission by $\sim$ 4 kpc in the south-east direction. We checked the astrometric accuracy of the HST images using stars in the field in the GAIA catalog (Gaia Collaboration et al., 2018), and this is not the source of the observed offset. Spatial offsets between the star-forming regions and [CII] line emission have been observed in other star-forming galaxies at $z \gtrsim 5$ (e.g., Carniani et al., 2018), and could be related to difference in the ionizing state of the gas, dust obscuration, and/or the effect of stellar feedback destroying molecular gas (e.g., Vallini et al., 2015; Katz et al., 2017). Given the large beam size of our observations (the projected size of the beam is roughly the size of the observed offset), it is hard to judge if the offset is due to physical reasons.

Together with the tentative detection of the [CII] line in GN-108036, we identify a potential additional system located approximately at 30 kpc in the east direction. The spectrum is shown in the lower-left panel of Figure 3.1.6. Interestingly, the tentative detection is at a similar velocity (-910 ± 57 km s^{-1}) of the possible detection of the [CII] line in GN-108036, but the line profile is significantly wider (503 ± 134 km s^{-1}). The integrated [CII] flux is 0.47$\pm$0.15 Jy km s^{-1}, which

corresponds to a tentative detection with a S/N of ≈ 3. As Figure A0.2 in the Appendix shows, the signal is much weaker in the compact array data. The contours of the integrated [CII] line emission from the extended array data are shown in green in the right panel of Figure 3.1.6.

Table 3.1.1 summarizes the [CII] line properties of the tentative detections of GN-108036 and the companion. We include the redshift of the source (Lyα and [CII]), the central velocity and FWHM of the [CII] line from the best 1-D Gaussian fit, the integrated [CII] flux, and the [CII] luminosity.

Chapter 4

Analysis

4.1 Relation between [CII] line emission and star formation activity

Under the assumption of an interstellar medium in thermal equilibrium, and considering that the [CII] transition is one of the main cooling channels (e.g., Wolfire et al., 2003), a tight relation is expected between the [CII] line emission and the star formation activity. This relation has been observed in nearby, star-forming galaxies and high-z, main-sequence systems (e.g., De Looze et al., 2014b; Herrera-Camus et al., 2015; Herrera-Camus et al., 2018; Schaerer et al., 2020). Fig. 4.1.1 shows the [CII] luminosity - SFR relation for star-forming galaxies detected at $z \gtrsim 6$ (Matthee et al., 2019). The solid (orange) and dot-dashed (blue) lines represent the best fit to star-forming galaxies on and above ($\times 20 - 100$) the main-sequence (corrected by the redshift dependence of the main-sequence; Herrera-Camus et al., 2018). GN-108036, with a SFR that ranges from ∼30 to 100 $M_{\odot}$ yr^{-1} (Ono et al., 2011), follows the main relation observed in other $z \gtrsim 6$ galaxies, and lies in between the [CII]−SFR scaling relations for galaxies on and above the main-sequence. Regarding the potential companion of GN-108036, there is no HST counterpart or SFR estimate available, so we include the [CII] luminosity value as an horizontal green line.

The fact that GN-108036 follows the [CII]−SFR relation observed in other $z \gtrsim 6$ star-forming galaxies, combined with the small spatial offset observed between the peak of the [CII] line and the rest-frame UV and Lyα emission, argues in favor of

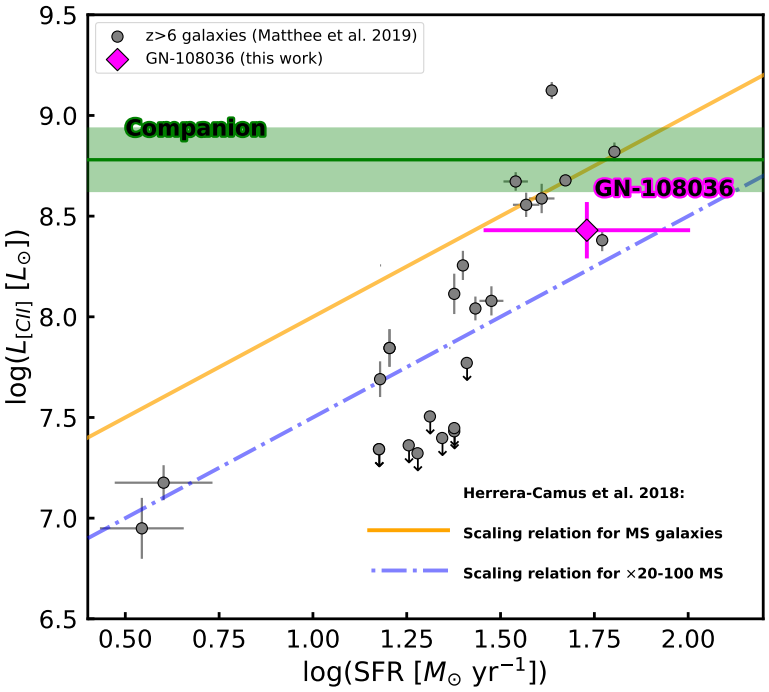

Figure 4.1.1: [CII] luminosity − SFR relation observed in $z \gtrsim 6$ galaxies (gray circles; Matthee et al., 2019). The solid (orange) and dot-dashed (blue) lines correspond to the scaling relations observed in star-forming galaxies on and above ($\times 20 - 100$) the main-sequence (Herrera-Camus et al., 2018). The tentative detection of GN-108036 is shown with a magenta diamond. The SFR of GN-108036 ranges from ≈ 30 to ≈ 100 $M_\odot$ year^{-1} depending if the rest-frame UV emission or SED are used, respectively (Ono et al., 2011). The green solid line indicates the [CII] luminosity for the companion, which does not have an HST counterpart or SFR estimate available.

the interpretation of the [CII] line detection in GN-108036 as real and associated with the galaxy.

4.2 Lyα - [CII] velocity offset

Lyα is a resonant line, thus its profile carries important information about the content, geometry and kinematics of the atomic gas. At $z \approx 2 - 3$, star-forming galaxies can show significant velocity differences between Lyα and non-resonant lines (e.g., Hα, Hβ, [Oiii]) that range between 100 to 1000 km s^{-1} (e.g., **??**). At $z \gtrsim 6$, Lyman Break galaxies show Lyα velocity offsets with respect to the [CII] line that are typically between 100 to 500 km s^{-1}. The record belongs to the star-forming galaxy B14-65666 at $z = 7.15$, with Lyα line emisison redshifted with respect to the [CII] and [OIII] lines by $\Delta v_{\mathrm{Ly}\alpha} = 772$ km s^{-1} (Hashimoto et al.,

2019).

In the case of GN-108036, the tentative detection of the [CII] line is blueshifted with respect to the Lyα line by 982.2 ± 12.7 km s^{-1}, the largest velocity offset reported to date for a system at $z \gtrsim 6$. Figure 4.2.1 compares the Lyα velocity offset in GN-108036 with star-forming galaxies at $z \gtrsim 6$ compiled by Hashimoto et al. (2019). The left panel shows the anti-correlation observed between $\Delta v_{\mathrm{Ly}\alpha}$ and Lyα equivalent width ($\mathrm{EW}_0(\mathrm{Ly}\alpha)$), and the right panel shows the positive correlation observed between $\Delta v_{\mathrm{Ly}\alpha}$ and the UV absolute magnitude (M_{UV}) of the system.

To first order, and based on models of Lyα radiative transfer in expanding shells, there are two scenarios that can explained the large velocity offset observed in GN-108036. In the first scenario, the presence of a large column density of atomic hydrogen implies that Lyα photons suffer from more dust attenuation due to a larger optical path length, which causes a reduction of the Lyα equivalent width and an increase in the Lyα velocity offset (e.g., Erb et al., 2014). In the second scenario, the increasing UV absolute magnitude is correlated with stronger star formation activity, which can drive outflows including atomic gas that would increase the Lyα velocity offset. In a simple approximation, it is expected that the velocity of the outflow (v_{out}) is correlated with $\Delta v_{\mathrm{Ly}\alpha}$ as $\Delta v_{\mathrm{Ly}\alpha} \sim 2 \times v_{\mathrm{out}}$ (e.g., **?**). This would imply an atomic gas outflow velocity for GN-108036 of ~ 500 km s^{-1}. This outflow velocity is consistent with those observed in local starburst with comparable levels of star formation activity (e.g., Heckman and Borthakur, 2016).

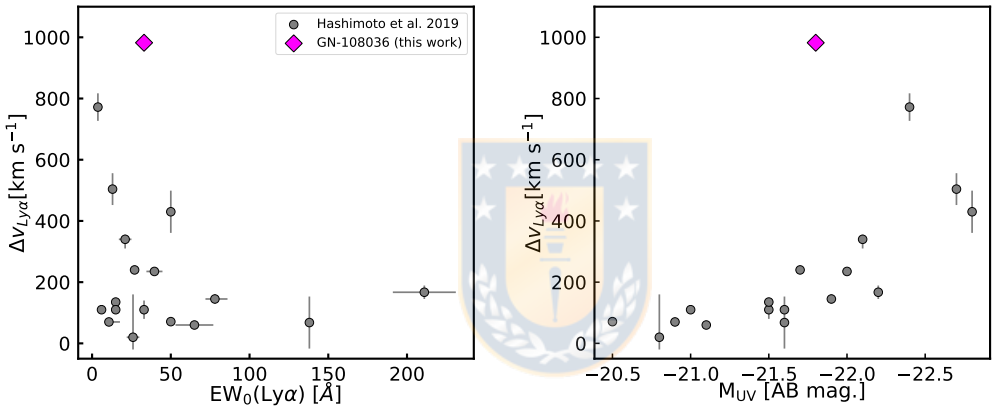

Figure 4.2.1: Lyα velocity offset ($\Delta v_{Ly\alpha}$) with respect to the [CII] line as a function of Lyα equivalent width (*left*) and absolute UV magnitude (*right*) observed in star-forming galaxies at $5 < z < 8$ (gray circles; Hashimoto et al., 2019). The tentative detection (3σ) of GN-108036 is shown in both panels with a pink diamond.

Chapter 5

Conclusions

We report new NOEMA Band 3 observations of the [CII] 158 μm transition and dust continuum in one of the most distant sources in the Northern hemisphere, the star-forming galaxy GN-108036 detected in Lyα emission at $z = 7.12$ (Ono et al., 2011). Our main results can be summarized as follows:

1. We tentatively detect GN-108036 in [CII] line emission with a $S/N \approx 3$. The peak of the integrated emission is spatially offset about ~ 4 kpc with respect to the peak of the rest-frame UV and Lyα line detection (Ono et al., 2011). Spatial offsets of similar magnitudes are commonly observed in star-forming systems at $z \gtrsim 6$ (e.g., Carniani et al., 2018). The potential [CII] detection is blueshifted with respect to the Lyα emission by 982.2 ± 12.7 km s^{-1}. If confirmed, this would be the largest Lya velocity offset reported to date for a $z \gtrsim 6$ star-forming galaxy. GN-108036 is not detected in the dust continuum, and the 3σ dust mass upper limit is $M_{\rm dust} < 9.5 \times 10^6\ M_\odot$.

2. Together with GN-108036, we tentatively detect (3σ) in [CII] line emission one additional source at similar systemic velocity but located ≈ 30 kpc east of GN-108036. This source has no counterpart in the HST imaging of the field.

3. GN-108036, with a SFR that ranges between $\sim 30 - 100\ M_\odot$ yr^{-1} (Ono et al., 2011), follows the relation between the [CII] luminosity and the SFR observed in star-forming galaxies at $z \gtrsim 6$ (e.g., Matthee et al., 2019), and lies in between the scaling relations of $L_{\rm [CII]} -$ SFR observed in star-forming

galaxies on and above $(20-100\times)$ the main-sequence of star-forming galaxies (removing the dependence with redshift; Herrera-Camus et al., 2018). The fact that the potential [CII] emission in GN-108036 is almost co-spatial with the rest-frame UV and Lyα emission, and that GN-108036 follows the $L_{[\mathrm{CII}]} - \mathrm{SFR}$ relation, argues in favor of the [CII] line detection to be real.

4. The Lyα velocity offset observed in GN-108036 is consistent with the positive and negative correlations observed between $\Delta v_{Ly\alpha}$ and $\mathrm{EW}_0(\mathrm{Ly}\alpha)$ and M_{UV} in $z \gtrsim 6$ star-forming galaxies, respectively. If models of Lyα radiative transfer in expanding shells apply to GN-108036, the physical scenarios that could explain the observed large Lya velocity offset, the low $\mathrm{EW}_0(\mathrm{Ly}\alpha)$ and high M_{UV} are: 1) the presence of a large HI column density, 2) the existence of an outflow with velocity $v_{\mathrm{out}} \sim \Delta v_{\mathrm{Ly}\alpha}/2 \sim 500$ km s^{-1}. Certainly deeper, higher angular resolutions observations of GN-108036 are needed to confirm the [CII] line detection, and further explore these two scenarios.

The upgraded NOEMA capabilities, which will have 12 antennas by the end of the summer of 2022, and has a correlator (*PolyFiX*) with a bandwidth of ~ 31 GHz, offers a great opportunity to search and detect in [CII] line emission $z \gtrsim 6$ galaxies based on robust photometric redshifts estimates. The latter should become available in large numbers in the near future thanks to the *James Webb Space Telescope*.

Reportamos nuevas observaciones de la transición [CII] 158 μm realizadas por NOEMA en la Banda 3 y en el continuo de polvo en una de las fuentes más distantes del hemisferio norte, la galaxia típica GN-108036 detectada con la emisión de Lyα a $z = 7.213$. Los resultados más importantes son los siguientes:

1. Tentativamente detectamos GN-108036 en la línea [CII] con una $S/N \approx 3$. El peak de la emisión integrada no coincide espacialmente por ~ 4 kpc respecto al peak en reposo de la detección de Lyα y UV (Ono et al., 2011). No coincidencia espaciales de magnitudes similares comunmente se observan en galaxias típicas a $z \gtrsim 6$ (e.g., Carniani et al., 2018). La potencial detección de [CII] está corrida hacia el azul con respecto a la emisión de Lyα por 982.2 ± 12.7 km s^{-1}. Si se confirma, esta sería la más grande diferencia en velocidad reportado hasta ahora para una galaxia típica a $z \gtrsim 6$. GN-108036 no está detectada en el continuo de polvo, y el límite superior 3σ de masa de polvo es $M_{\rm dust} < 9.5 \times 10^6\ M_\odot$.

2. Junto con GN-108036, tentativamente detectamos (3σ) en la línea de emisión [CII] una fuente adicional a similar velocidad sistémica pero localizada $\approx$ 30 kpc al este de GN-108036. Esta fuente no tiene una contraparte en el campo de visión de HST.

3. GN-108036, con una SFR que oscila entre $\sim 30 - 100\ M_\odot$ yr^{-1} (Ono et al., 2011), sigue la relación entre la luminosidad de [CII] y SFR observada en galaxias típicas a $z \gtrsim 6$ (e.g., Matthee et al., 2019), y se encuentra dentro de la relación entre $L_{\rm [CII]} -$ SFR observada en galaxias típicas en y por encima $(20 - 100\times)$ de la secuencia principal para galaxias típicas (removiendo la dependencia con el redshift Herrera-Camus et al., 2018). El hecho de que la potencial emisión de [CII] en GN-108036 es casi coespacial con la emisión en reposo de Lyα y UV, y que GN-108036 sigue la relación $L_{\rm [CII]} -$ SFR, argumenta en favor de la detección de la línea [CII] para ser real.

4. La diferencia en velocidad respecto a la línea de Lyα observada en GN-108036 es consistente con la correlación positiva y negativa observada entre $\Delta v_{Ly\alpha}$ y EW$_0$(Lyα) y $M_{\rm UV}$ en galaxia típicas a $z \gtrsim 6$, respectivamente. Si a GN-108036 se le aplican modelos de transferencia de radiación de Lyα en cáscaras expansivas, los escenarios físicos que podrían explicar el gran valor en diferencia de velocidad observado, el bajo valor de EW$_0$(Lyα) y el alto

valor de $M_{\rm UV}$ son: 1) la presencia de una gran densidad de columna de [HI], 2) la existencia de un outflow con una velocidad $v_{\rm out} \sim \Delta v_{{\rm Ly}\alpha}/2 \sim 500$ km s^{-1}. Ciertamente más profundo, observaciones con mayor resolución angular de GN-108036 son necesarias para confirmar la detección de la línea de [CII], y explorar más a fondo estos dos escenarios.

Las capacidades mejoradas de NOEMA, que tendrá 12 antenas para fines del verano de 2022 y tiene un correlador (*PolyFiX*) con un ancho de banda de ~ 31 GHz, ofrece una gran oportunidad para buscar y detectar en la emisión [CII] galaxias a $z \gtrsim 6$ basado en robustas estimaciones de redshift fotométrico. Esto último debería estar disponible en grandes cantidades en un futuro próximo gracias al *telescopio espacial James Webb*.

Bibliography

Bañados, E., Venemans, B. P., Mazzucchelli, C., Farina, E. P., Walter, F., Wang, F., Decarli, R., Stern, D., Fan, X., Davies, F. B., Hennawi, J. F., Simcoe, R. A., Turner, M. L., Rix, H.-W., Yang, J., Kelson, D. D., Rudie, G. C., and Winters, J. M. (2018). An 800-million-solar-mass black hole in a significantly neutral Universe at a redshift of 7.5. , 553(7689):473–476.

Bouwens, R., Smit, R., Schouws, S., Stefanon, M., Bowler, R., Endsley, R., Gonzalez, V., Inami, H., Stark, D., Oesch, P., et al. (2021). Reionization era bright emission line survey: selection and characterization of luminous interstellar medium reservoirs in the z> 6.5 universe. *arXiv preprint arXiv:2106.13719*.

Bromm, V. and Yoshida, N. (2011). The First Galaxies. , 49(1):373–407.

Carniani, S., Ferrara, A., Maiolino, R., Castellano, M., Gallerani, S., Fontana, A., Kohandel, M., Lupi, A., Pallottini, A., Pentericci, L., Vallini, L., and Vanzella, E. (2020). Missing [C II] emission from early galaxies. , 499(4):5136–5150.

Carniani, S., Maiolino, R., Smit, R., and Amorín, R. (2018). ALMA Detection of Extended [C II] Emission in Himiko at z = 6.6. , 854(1):L7.

Cigan, P., Young, L., Cormier, D., Lebouteiller, V., Hunter, D. A., Madden, S., and Little Things (2015). Herschel's View of LITTLE THINGS Metal-Poor Dwarf Galaxies. In *American Astronomical Society Meeting Abstracts #225*, volume 225 of *American Astronomical Society Meeting Abstracts*, page 212.08.

Cormier, D. (2014). Disentangling the ISM phases of the nearby low-metallicity dwarf galaxy NGC4214 using velocity-resolved [CII]. SOFIA Proposal.

Dayal, P. and Ferrara, A. (2018). Early galaxy formation and its large-scale effects. , 780:1–64.

De Looze, I., Cormier, D., Lebouteiller, V., Madden, S., Baes, M., Bendo, G. J., Boquien, M., Boselli, A., Clements, D. L., Cortese, L., Cooray, A., Galametz, M., Galliano, F., Graciá-Carpio, J., Isaak, K., Karczewski, O. Ł., Parkin, T. J., Pellegrini, E. W., Rémy-Ruyer, A., Spinoglio, L., Smith, M. W. L., and Sturm, E. (2014a). The applicability of far-infrared fine-structure lines as star formation rate tracers over wide ranges of metallicities and galaxy types. , 568:A62.

De Looze, I., Cormier, D., Lebouteiller, V., Madden, S., Baes, M., Bendo, G. J.,

Boquien, M., Boselli, A., Clements, D. L., Cortese, L., Cooray, A., Galametz, M., Galliano, F., Graciá-Carpio, J., Isaak, K., Karczewski, O. Ł., Parkin, T. J., Pellegrini, E. W., Rémy-Ruyer, A., Spinoglio, L., Smith, M. W. L., and Sturm, E. (2014b). The applicability of far-infrared fine-structure lines as star formation rate tracers over wide ranges of metallicities and galaxy types. , 568:A62.

Dijkstra, M. (2017). Saas-fee lecture notes: physics of lyman alpha radiative transfer. *arXiv preprint arXiv:1704.03416*.

Dunne, L., Eales, S., Edmunds, M., Ivison, R., Alexander, P., and Clements, D. L. (2000). The SCUBA Local Universe Galaxy Survey - I. First measurements of the submillimetre luminosity and dust mass functions. , 315(1):115–139.

Endsley, R. and Stark, D. P. (2021). Strong Lyα Emission in an Overdense Region at $z = 6.8$: A Very Large ($R \sim 3$ physical Mpc) Ionized Bubble in COSMOS? *arXiv e-prints*, page arXiv:2112.14779.

Erb, D. K., Steidel, C. C., Trainor, R. F., Bogosavljević, M., Shapley, A. E., Nestor, D. B., Kulas, K. R., Law, D. R., Strom, A. L., Rudie, G. C., Reddy, N. A., Pettini, M., Konidaris, N. P., Mace, G., Matthews, K., and McLean, I. S. (2014). The Lyα Properties of Faint Galaxies at z ~2-3 with Systemic Redshifts and Velocity Dispersions from Keck-MOSFIRE. , 795(1):33.

Faber, S. M., Phillips, A. C., Kibrick, R. I., Alcott, B., Allen, S. L., Burrous, J., Cantrall, T., Clarke, D., Coil, A. L., Cowley, D. J., Davis, M., Deich, W. T. S., Dietsch, K., Gilmore, D. K., Harper, C. A., Hilyard, D. F., Lewis, J. P., McVeigh, M., Newman, J., Osborne, J., Schiavon, R., Stover, R. J., Tucker, D., Wallace, V., Wei, M., Wirth, G., and Wright, C. A. (2003). The DEIMOS spectrograph for the Keck II Telescope: integration and testing. In Iye, M. and Moorwood, A. F. M., editors, *Instrument Design and Performance for Optical/Infrared Ground-based Telescopes*, volume 4841 of *Society of Photo-Optical Instrumentation Engineers (SPIE) Conference Series*, pages 1657–1669.

Faisst, A. L., Fudamoto, Y., Oesch, P. A., Scoville, N., Riechers, D. A., Pavesi, R., and Capak, P. (2020). ALMA characterizes the dust temperature of z $\sim$ 5.5 star-forming galaxies. , 498(3):4192–4204.

Fan, X., Carilli, C., and Keating, B. (2006a). Observational constraints on cosmic reionization. *Annu. Rev. Astron. Astrophys.*, 44:415–462.

Fan, X., Strauss, M. A., Becker, R. H., White, R. L., Gunn, J. E., Knapp, G. R., Richards, G. T., Schneider, D. P., Brinkmann, J., and Fukugita, M. (2006b). Constraining the evolution of the ionizing background and the epoch of reionization with z 6 quasars. ii. a sample of 19 quasars. *The Astronomical Journal*, 132(1):117.

Fujimoto, S., Silverman, J. D., Bethermin, M., Ginolfi, M., Jones, G. C., Le Fèvre, O., Dessauges-Zavadsky, M., Rujopakarn, W., Faisst, A. L., Fudamoto, Y., Cassata, P., Morselli, L., Maiolino, R., Schaerer, D., Capak, P., Yan, L., Vallini, L., Toft, S., Loiacono, F., Zamorani, G., Talia, M., Narayanan, D.,

Hathi, N. P., Lemaux, B. C., Boquien, M., Amorin, R., Ibar, E., Koekemoer, A. M., Méndez-Hernández, H., Bardelli, S., Vergani, D., Zucca, E., Romano, M., and Cimatti, A. (2020). The ALPINE-ALMA [C II] Survey: Size of Individual Star-forming Galaxies at z = 4-6 and Their Extended Halo Structure. , 900(1):1.

Gaia Collaboration, Brown, A. G. A., Vallenari, A., Prusti, T., de Bruijne, J. H. J., Babusiaux, C., Bailer-Jones, C. A. L., Biermann, M., Evans, D. W., Eyer, L., Jansen, F., Jordi, C., Klioner, S. A., Lammers, U., Lindegren, L., Luri, X., Mignard, F., Panem, C., Pourbaix, D., Randich, S., Sartoretti, P., Siddiqui, H. I., Soubiran, C., van Leeuwen, F., Walton, N. A., Arenou, F., Bastian, U., Cropper, M., Drimmel, R., Katz, D., Lattanzi, M. G., Bakker, J., Cacciari, C., Castañeda, J., Chaoul, L., Cheek, N., De Angeli, F., Fabricius, C., Guerra, R., Holl, B., Masana, E., Messineo, R., Mowlavi, N., Nienartowicz, K., Panuzzo, P., Portell, J., Riello, M., Seabroke, G. M., Tanga, P., Thévenin, F., Gracia-Abril, G., Comoretto, G., Garcia-Reinaldos, M., Teyssier, D., Altmann, M., Andrae, R., Audard, M., Bellas-Velidis, I., Benson, K., Berthier, J., Blomme, R., Burgess, P., Busso, G., Carry, B., Cellino, A., Clementini, G., Clotet, M., Creevey, O., Davidson, M., De Ridder, J., Delchambre, L., Dell'Oro, A., Ducourant, C., Fernández-Hernández, J., Fouesneau, M., Frémat, Y., Galluccio, L., García-Torres, M., González-Núñez, J., González-Vidal, J. J., Gosset, E., Guy, L. P., Halbwachs, J. L., Hambly, N. C., Harrison, D. L., Hernández, J., Hestroffer, D., Hodgkin, S. T., Hutton, A., Jasniewicz, G., Jean-Antoine-Piccolo, A., Jordan, S., Korn, A. J., Krone-Martins, A., Lanzafame, A. C., Lebzelter, T., Löffler, W., Manteiga, M., Marrese, P. M., Martín-Fleitas, J. M., Moitinho, A., Mora, A., Muinonen, K., Osinde, J., Pancino, E., Pauwels, T., Petit, J. M., Recio-Blanco, A., Richards, P. J., Rimoldini, L., Robin, A. C., Sarro, L. M., Siopis, C., Smith, M., Sozzetti, A., Süveges, M., Torra, J., van Reeven, W., Abbas, U., Abreu Aramburu, A., Accart, S., Aerts, C., Altavilla, G., Álvarez, M. A., Alvarez, R., Alves, J., Anderson, R. I., Andrei, A. H., Anglada Varela, E., Antiche, E., Antoja, T., Arcay, B., Astraatmadja, T. L., Bach, N., Baker, S. G., Balaguer-Núñez, L., Balm, P., Barache, C., Barata, C., Barbato, D., Barblan, F., Barklem, P. S., Barrado, D., Barros, M., Barstow, M. A., Bartholomé Muñoz, S., Bassilana, J. L., Becciani, U., Bellazzini, M., Berihuete, A., Bertone, S., Bianchi, L., Bienaymé, O., Blanco-Cuaresma, S., Boch, T., Boeche, C., Bombrun, A., Borrachero, R., Bossini, D., Bouquillon, S., Bourda, G., Bragaglia, A., Bramante, L., Breddels, M. A., Bressan, A., Brouillet, N., Brüsemeister, T., Brugaletta, E., Bucciarelli, B., Burlacu, A., Busonero, D., Butkevich, A. G., Buzzi, R., Caffau, E., Cancelliere, R., Cannizzaro, G., Cantat-Gaudin, T., Carballo, R., Carlucci, T., Carrasco, J. M., Casamiquela, L., Castellani, M., Castro-Ginard, A., Charlot, P., Chemin, L., Chiavassa, A., Cocozza, G., Costigan, G., Cowell, S., Crifo, F., Crosta, M., Crowley, C., Cuypers, J., Dafonte, C., Damerdji, Y., Dapergolas, A., David, P., David, M., de Laverny, P., De Luise, F., De March, R., de Martino, D., de Souza, R., de Torres, A., Debosscher, J., del Pozo, E., Delbo, M., Delgado, A., Delgado, H. E., Di Matteo, P., Diakite, S., Diener, C., Distefano, E., Dolding, C., Drazinos, P., Durán, J., Edvardsson, B., Enke, H., Eriksson, K., Esquej, P., Eynard Bontemps, G., Fabre, C., Fabrizio, M., Faigler,

S., Falcão, A. J., Farràs Casas, M., Federici, L., Fedorets, G., Fernique, P., Figueras, F., Filippi, F., Findeisen, K., Fonti, A., Fraile, E., Fraser, M., Frézouls, B., Gai, M., Galleti, S., Garabato, D., García-Sedano, F., Garofalo, A., Garralda, N., Gavel, A., Gavras, P., Gerssen, J., Geyer, R., Giacobbe, P., Gilmore, G., Girona, S., Giuffrida, G., Glass, F., Gomes, M., Granvik, M., Gueguen, A., Guerrier, A., Guiraud, J., Gutiérrez-Sánchez, R., Haigron, R., Hatzidimitriou, D., Hauser, M., Haywood, M., Heiter, U., Helmi, A., Heu, J., Hilger, T., Hobbs, D., Hofmann, W., Holland, G., Huckle, H. E., Hypki, A., Icardi, V., Janßen, K., Jevardat de Fombelle, G., Jonker, P. G., Juhász, Á. L., Julbe, F., Karampelas, A., Kewley, A., Klar, J., Kochoska, A., Kohley, R., Kolenberg, K., Kontizas, M., Kontizas, E., Koposov, S. E., Kordopatis, G., Kostrzewa-Rutkowska, Z., Koubsky, P., Lambert, S., Lanza, A. F., Lasne, Y., Lavigne, J. B., Le Fustec, Y., Le Poncin-Lafitte, C., Lebreton, Y., Leccia, S., Leclerc, N., Lecoeur-Taibi, I., Lenhardt, H., Leroux, F., Liao, S., Licata, E., Lindstrøm, H. E. P., Lister, T. A., Livanou, E., Lobel, A., López, M., Managau, S., Mann, R. G., Mantelet, G., Marchal, O., Marchant, J. M., Marconi, M., Marinoni, S., Marschalkó, G., Marshall, D. J., Martino, M., Marton, G., Mary, N., Massari, D., Matijevič, G., Mazeh, T., McMillan, P. J., Messina, S., Michalik, D., Millar, N. R., Molina, D., Molinaro, R., Molnár, L., Montegriffo, P., Mor, R., Morbidelli, R., Morel, T., Morris, D., Mulone, A. F., Muraveva, T., Musella, I., Nelemans, G., Nicastro, L., Noval, L., O'Mullane, W., Ordénovic, C., Ordóñez-Blanco, D., Osborne, P., Pagani, C., Pagano, I., Pailler, F., Palacin, H., Palaversa, L., Panahi, A., Pawlak, M., Piersimoni, A. M., Pineau, F. X., Plachy, E., Plum, G., Poggio, E., Poujoulet, E., Prša, A., Pulone, L., Racero, E., Ragaini, S., Rambaux, N., Ramos-Lerate, M., Regibo, S., Reylé, C., Riclet, F., Ripepi, V., Riva, A., Rivard, A., Rixon, G., Roegiers, T., Roelens, M., Romero-Gómez, M., Rowell, N., Royer, F., Ruiz-Dern, L., Sadowski, G., Sagristà Sellés, T., Sahlmann, J., Salgado, J., Salguero, E., Sanna, N., Santana-Ros, T., Sarasso, M., Savietto, H., Schultheis, M., Sciacca, E., Segol, M., Segovia, J. C., Ségransan, D., Shih, I. C., Siltala, L., Silva, A. F., Smart, R. L., Smith, K. W., Solano, E., Solitro, F., Sordo, R., Soria Nieto, S., Souchay, J., Spagna, A., Spoto, F., Stampa, U., Steele, I. A., Steidelmüller, H., Stephenson, C. A., Stoev, H., Suess, F. F., Surdej, J., Szabados, L., Szegedi-Elek, E., Tapiador, D., Taris, F., Tauran, G., Taylor, M. B., Teixeira, R., Terrett, D., Teyssandier, P., Thuillot, W., Titarenko, A., Torra Clotet, F., Turon, C., Ulla, A., Utrilla, E., Uzzi, S., Vaillant, M., Valentini, G., Valette, V., van Elteren, A., Van Hemelryck, E., van Leeuwen, M., Vaschetto, M., Vecchiato, A., Veljanoski, J., Viala, Y., Vicente, D., Vogt, S., von Essen, C., Voss, H., Votruba, V., Voutsinas, S., Walmsley, G., Weiler, M., Wertz, O., Wevers, T., Wyrzykowski, Ł., Yoldas, A., Žerjal, M., Ziaeepour, H., Zorec, J., Zschocke, S., Zucker, S., Zurbach, C., and Zwitter, T. (2018). Gaia Data Release 2. Summary of the contents and survey properties. , 616:A1.

Giavalisco, M. (2002). Lyman-Break Galaxies. , 40:579–641.

Glazebrook, K., Schreiber, C., Labbé, I., Nanayakkara, T., Kacprzak, G. G., Oesch, P. A., Papovich, C., Spitler, L. R., Straatman, C. M. S., Tran, K.-V. H.,

and Yuan, T. (2017). A massive, quiescent galaxy at a redshift of 3.717. , 544(7648):71–74.

Goldsmith, P. F., Langer, W. D., Pineda, J. L., and Velusamy, T. (2012). Collisional Excitation of the [C II] Fine Structure Transition in Interstellar Clouds. , 203(1):13.

Greig, B. and Mesinger, A. (2017). Simultaneously constraining the astrophysics of reionization and the epoch of heating with 21CMMC. , 472(3):2651–2669.

Guilloteau, S. and Lucas, R. (2000). Imaging at the IRAM Plateau de Bure Interferometer. In Mangum, J. G. and Radford, S. J. E., editors, *Imaging at Radio through Submillimeter Wavelengths*, volume 217 of *Astronomical Society of the Pacific Conference Series*, page 299.

Hashimoto, T., Inoue, A. K., Mawatari, K., Tamura, Y., Matsuo, H., Furusawa, H., Harikane, Y., Shibuya, T., Knudsen, K. K., Kohno, K., et al. (2019). Big three dragons: A z= 7.15 lyman-break galaxy detected in [o iii] 88 μm,[c ii] 158 μm, and dust continuum with alma. *Publications of the Astronomical Society of Japan*, 71(4):71.

Hashimoto, T., Ouchi, M., Shimasaku, K., Ono, Y., Nakajima, K., Rauch, M., Lee, J., and Okamura, S. (2013). Erratum: "Gas Motion Study of Lyα Emitters at z ~2 Using Far-ultraviolet and Optical Spectral Lines" <A href="/abs/2013ApJ...765...70H">(2013, ApJ, 765, 70)</A>. , 775(2):140.

Heckman, T. M. and Borthakur, S. (2016). The Implications of Extreme Outflows from Extreme Starbursts. , 822(1):9.

Herrera-Camus, R., Bolatto, A. D., Wolfire, M. G., Smith, J. D., Croxall, K. V., Kennicutt, R. C., Calzetti, D., Helou, G., Walter, F., Leroy, A. K., Draine, B., Brandl, B. R., Armus, L., Sandstrom, K. M., Dale, D. A., Aniano, G., Meidt, S. E., Boquien, M., Hunt, L. K., Galametz, M., Tabatabaei, F. S., Murphy, E. J., Appleton, P., Roussel, H., Engelbracht, C., and Beirao, P. (2015). [C II] 158 μm Emission as a Star Formation Tracer. , 800:1.

Herrera-Camus, R., Förster Schreiber, N., Genzel, R., Tacconi, L., Bolatto, A., Davies, R. L., Fisher, D., Lutz, D., Naab, T., Shimizu, T., Tadaki, K., and Übler, H. (2021). Kiloparsec view of a typical star-forming galaxy when the Universe was $\sim$1 Gyr old. I. Properties of outflow, halo, and interstellar medium. , 649:A31.

Herrera-Camus, R., Sturm, E., Graciá-Carpio, J., Lutz, D., Contursi, A., Veilleux, S., Fischer, J., González-Alfonso, E., Poglitsch, A., Tacconi, L., et al. (2018). Shining, a survey of far-infrared lines in nearby galaxies. ii. line-deficit models, agn impact,[c ii]–sfr scaling relations, and mass–metallicity relation in (u) lirgs. *The Astrophysical Journal*, 861(2):95.

Illingworth, G. (1999). Galaxies at high redshift. *Astrophysics and Space Science*, 269:165–181.

Isobe, T., Feigelson, E. D., Akritas, M. G., and Babu, G. J. (1990). Linear Regression in Astronomy. I. , 364:104.

Israel, F. P. and Maloney, P. R. (2011). [CII] emission from the Magellanic Clouds. In Röllig, M., Simon, R., Ossenkopf, V., and Stutzki, J., editors, *EAS Publications Series*, volume 52 of *EAS Publications Series*, pages 287–288.

Jiang, L., Egami, E., Fan, X., Windhorst, R. A., Cohen, S. H., Davé, R., Finlator, K., Kashikawa, N., Mechtley, M., Ouchi, M., and Shimasaku, K. (2013). Physical Properties of Spectroscopically Confirmed Galaxies at z >= 6. II. Morphology of the Rest-frame UV Continuum and Lyα Emission. , 773(2):153.

Jiang, L., Kashikawa, N., Wang, S., Walth, G., Ho, L. C., Cai, Z., Egami, E., Fan, X., Ito, K., Liang, Y., Schaerer, D., and Stark, D. P. (2021). Evidence for GN-z11 as a luminous galaxy at redshift 10.957. *Nature Astronomy*, 5:256–261.

Katz, H., Kimm, T., Sijacki, D., and Haehnelt, M. G. (2017). Interpreting ALMA observations of the ISM during the epoch of reionization. , 468(4):4831–4861.

Maiolino, R., Carniani, S., Fontana, A., Vallini, L., Pentericci, L., Ferrara, A., Vanzella, E., Grazian, A., Gallerani, S., Castellano, M., Cristiani, S., Brammer, G., Santini, P., Wagg, J., and Williams, R. (2015). The assembly of 'normal' galaxies at z $\sim$ 7 probed by ALMA. , 452(1):54–68.

Marrone, D. P., Spilker, J. S., Hayward, C. C., Vieira, J. D., Aravena, M., Ashby, M. L. N., Bayliss, M. B., Béthermin, M., Brodwin, M., Bothwell, M. S., Carlstrom, J. E., Chapman, S. C., Chen, C.-C., Crawford, T. M., Cunningham, D. J. M., De Breuck, C., Fassnacht, C. D., Gonzalez, A. H., Greve, T. R., Hezaveh, Y. D., Lacaille, K., Litke, K. C., Lower, S., Ma, J., Malkan, M., Miller, T. B., Morningstar, W. R., Murphy, E. J., Narayanan, D., Phadke, K. A., Rotermund, K. M., Sreevani, J., Stalder, B., Stark, A. A., Strandet, M. L., Tang, M., and Weiß, A. (2018). Galaxy growth in a massive halo in the first billion years of cosmic history. , 553(7686):51–54.

Matthee, J., Sobral, D., Boogaard, L. A., Röttgering, H., Vallini, L., Ferrara, A., Paulino-Afonso, A., Boone, F., Schaerer, D., and Mobasher, B. (2019). Resolved UV and [C II] Structures of Luminous Galaxies within the Epoch of Reionization. , 881(2):124.

Ning, Y., Jiang, L., Zheng, Z.-Y., and Wu, J. (2021). The Magellan M2FS Spectroscopic Survey of High-z Galaxies: Ly{} Emitters at $z \approx 6.6$ and the Evolution of Ly{} Luminosity Function over $z \approx 5.7 - 6.6$. *arXiv e-prints*, page arXiv:2112.07800.

Oesch, P. A., Brammer, G., van Dokkum, P. G., Illingworth, G. D., Bouwens, R. J., Labbé, I., Franx, M., Momcheva, I., Ashby, M. L. N., Fazio, G. G., Gonzalez, V., Holden, B., Magee, D., Skelton, R. E., Smit, R., Spitler, L. R., Trenti, M., and Willner, S. P. (2016). A Remarkably Luminous Galaxy at z=11.1 Measured with Hubble Space Telescope Grism Spectroscopy. , 819(2):129.

Ono, Y., Ouchi, M., Mobasher, B., Dickinson, M., Penner, K., Shimasaku, K., Weiner, B. J., Kartaltepe, J. S., Nakajima, K., Nayyeri, H., et al. (2011). Spectroscopic confirmation of three z-dropout galaxies at z= 6.844-7.213: Demographics of lyα emission in z 7 galaxies. *The Astrophysical Journal*, 744(2):83.

Ota, K., Iye, M., Kashikawa, N., Konno, A., Nakata, F., Totani, T., Kobayashi, M. A., Fudamoto, Y., Seko, A., Toshikawa, J., et al. (2017). A new constraint on reionization from the evolution of the lyα luminosity function at z 6–7 probed by a deep census of z= 7.0 lyα emitter candidates to 0.3 l. *The Astrophysical Journal*, 844(1):85.

Ota, K., Walter, F., Ohta, K., Hatsukade, B., Carilli, C. L., Da Cunha, E., González-López, J., Decarli, R., Hodge, J. A., Nagai, H., et al. (2014). Alma observation of 158 μm [c ii] line and dust continuum of az= 7 normally star-forming galaxy in the epoch of reionization. *The Astrophysical Journal*, 792(1):34.

Ouchi, M., Mobasher, B., Shimasaku, K., Ferguson, H. C., Fall, S. M., Ono, Y., Kashikawa, N., Morokuma, T., Nakajima, K., Okamura, S., Dickinson, M., Giavalisco, M., and Ohta, K. (2009). Large Area Survey for z = 7 Galaxies in SDF and GOODS-N: Implications for Galaxy Formation and Cosmic Reionization. , 706(2):1136–1151.

Planck Collaboration, Aghanim, N., Akrami, Y., Ashdown, M., Aumont, J., Baccigalupi, C., Ballardini, M., Banday, A. J., Barreiro, R. B., Bartolo, N., Basak, S., Battye, R., Benabed, K., Bernard, J. P., Bersanelli, M., Bielewicz, P., Bock, J. J., Bond, J. R., Borrill, J., Bouchet, F. R., Boulanger, F., Bucher, M., Burigana, C., Butler, R. C., Calabrese, E., Cardoso, J. F., Carron, J., Challinor, A., Chiang, H. C., Chluba, J., Colombo, L. P. L., Combet, C., Contreras, D., Crill, B. P., Cuttaia, F., de Bernardis, P., de Zotti, G., Delabrouille, J., Delouis, J. M., Di Valentino, E., Diego, J. M., Doré, O., Douspis, M., Ducout, A., Dupac, X., Dusini, S., Efstathiou, G., Elsner, F., Enßlin, T. A., Eriksen, H. K., Fantaye, Y., Farhang, M., Fergusson, J., Fernandez-Cobos, R., Finelli, F., Forastieri, F., Frailis, M., Fraisse, A. A., Franceschi, E., Frolov, A., Galeotta, S., Galli, S., Ganga, K., Génova-Santos, R. T., Gerbino, M., Ghosh, T., González-Nuevo, J., Górski, K. M., Gratton, S., Gruppuso, A., Gudmundsson, J. E., Hamann, J., Handley, W., Hansen, F. K., Herranz, D., Hildebrandt, S. R., Hivon, E., Huang, Z., Jaffe, A. H., Jones, W. C., Karakci, A., Keihänen, E., Keskitalo, R., Kiiveri, K., Kim, J., Kisner, T. S., Knox, L., Krachmalnicoff, N., Kunz, M., Kurki-Suonio, H., Lagache, G., Lamarre, J. M., Lasenby, A., Lattanzi, M., Lawrence, C. R., Le Jeune, M., Lemos, P., Lesgourgues, J., Levrier, F., Lewis, A., Liguori, M., Lilje, P. B., Lilley, M., Lindholm, V., López-Caniego, M., Lubin, P. M., Ma, Y. Z., Macías-Pérez, J. F., Maggio, G., Maino, D., Mandolesi, N., Mangilli, A., Marcos-Caballero, A., Maris, M., Martin, P. G., Martinelli, M., Martínez-González, E., Matarrese, S., Mauri, N., McEwen, J. D., Meinhold, P. R., Melchiorri, A., Mennella, A., Migliaccio, M., Millea, M., Mitra, S., Miville-

Deschênes, M. A., Molinari, D., Montier, L., Morgante, G., Moss, A., Natoli, P., Nørgaard-Nielsen, H. U., Pagano, L., Paoletti, D., Partridge, B., Patanchon, G., Peiris, H. V., Perrotta, F., Pettorino, V., Piacentini, F., Polastri, L., Polenta, G., Puget, J. L., Rachen, J. P., Reinecke, M., Remazeilles, M., Renzi, A., Rocha, G., Rosset, C., Roudier, G., Rubiño-Martín, J. A., Ruiz-Granados, B., Salvati, L., Sandri, M., Savelainen, M., Scott, D., Shellard, E. P. S., Sirignano, C., Sirri, G., Spencer, L. D., Sunyaev, R., Suur-Uski, A. S., Tauber, J. A., Tavagnacco, D., Tenti, M., Toffolatti, L., Tomasi, M., Trombetti, T., Valenziano, L., Valiviita, J., Van Tent, B., Vibert, L., Vielva, P., Villa, F., Vittorio, N., Wandelt, B. D., Wehus, I. K., White, M., White, S. D. M., Zacchei, A., and Zonca, A. (2020). Planck 2018 results. VI. Cosmological parameters. , 641:A6.

Robertson, B. E., Ellis, R. S., Furlanetto, S. R., and Dunlop, J. S. (2015). Cosmic reionization and early star-forming galaxies: A joint analysis of new constraints from planck and the hubble space telescope. *The Astrophysical Journal Letters*, 802(2):L19.

Schaerer, D., Ginolfi, M., Béthermin, M., Fudamoto, Y., Oesch, P. A., Le Fèvre, O., Faisst, A., Capak, P., Cassata, P., Silverman, J. D., Yan, L., Jones, G. C., Amorin, R., Bardelli, S., Boquien, M., Cimatti, A., Dessauges-Zavadsky, M., Giavalisco, M., Hathi, N. P., Fujimoto, S., Ibar, E., Koekemoer, A., Lagache, G., Lemaux, B. C., Loiacono, F., Maiolino, R., Narayanan, D., Morselli, L., Méndez-Hernàndez, H., Pozzi, F., Riechers, D., Talia, M., Toft, S., Vallini, L., Vergani, D., Zamorani, G., and Zucca, E. (2020). The ALPINE-ALMA [C II] survey. Little to no evolution in the [C II]-SFR relation over the last 13 Gyr. , 643:A3.

Schouws, S., Stefanon, M., Bouwens, R. J., Smit, R., Hodge, J. A., Labbé, I., Algera, H. S., Boogaard, L., Carniani, S., Fudamoto, Y., Holwerda, B. W., Illingworth, G. D., Maiolino, R., Maseda, M. V., Oesch, P. A., and van der Werf, P. P. (2021). Significant Dust-Obscured Star Formation in Luminous Lyman-break Galaxies at $z\sim7-8$. *arXiv e-prints*, page arXiv:2105.12133.

Schreiber, C., Elbaz, D., Pannella, M., Ciesla, L., Wang, T., and Franco, M. (2018). Dust temperature and mid-to-total infrared color distributions for star-forming galaxies at $0 < z < 4$. , 609:A30.

Smit, R. (2018). [CII] observations of galaxies in the Epoch of Reionization. In *The Growth of Galaxies in the Early Universe - IV*, page 40.

Stark, D. P., Ellis, R. S., Charlot, S., Chevallard, J., Tang, M., Belli, S., Zitrin, A., Mainali, R., Gutkin, J., Vidal-García, A., Bouwens, R., and Oesch, P. (2017). Lyα and C III] emission in z = 7-9 Galaxies: accelerated reionization around luminous star-forming systems? , 464(1):469–479.

Steidel, C. C., Giavalisco, M., Pettini, M., Dickinson, M., and Adelberger, K. L. (1996). Spectroscopic Confirmation of a Population of Normal Star-forming Galaxies at Redshifts $Z > 3$. , 462:L17.

Strandet, M. L., Weiss, A., De Breuck, C., Marrone, D. P., Vieira, J. D., Aravena, M., Ashby, M. L. N., Béthermin, M., Bothwell, M. S., Bradford, C. M., Carlstrom, J. E., Chapman, S. C., Cunningham, D. J. M., Chen, C.-C., Fassnacht, C. D., Gonzalez, A. H., Greve, T. R., Gullberg, B., Hayward, C. C., Hezaveh, Y., Litke, K., Ma, J., Malkan, M., Menten, K. M., Miller, T., Murphy, E. J., Narayanan, D., Phadke, K. A., Rotermund, K. M., Spilker, J. S., and Sreevani, J. (2017). ISM Properties of a Massive Dusty Star-forming Galaxy Discovered at z $\sim$ 7. , 842(2):L15.

Thomas, R. M., Zaroubi, S., Ciardi, B., Pawlik, A. H., Labropoulos, P., Jelić, V., Bernardi, G., Brentjens, M. A., de Bruyn, A. G., Harker, G. J. A., Koopmans, L. V. E., Mellema, G., Pandey, V. N., Schaye, J., and Yatawatta, S. (2009). Fast large-scale reionization simulations. , 393(1):32–48.

Vallini, L., Gallerani, S., Ferrara, A., and Baek, S. (2013). Far-infrared line emission from high-redshift galaxies. , 433(2):1567–1572.

Vallini, L., Gallerani, S., Ferrara, A., Pallottini, A., and Yue, B. (2015). On the [CII]-SFR Relation in High Redshift Galaxies. , 813:36.

Venemans, B. P., Neeleman, M., Walter, F., Novak, M., Decarli, R., Hennawi, J. F., and Rix, H.-W. (2019). 400 pc Imaging of a Massive Quasar Host Galaxy at a Redshift of 6.6. , 874(2):L30.

Venemans, B. P., Walter, F., Neeleman, M., Novak, M., Otter, J., Decarli, R., Bañados, E., Drake, A., Farina, E. P., Kaasinen, M., Mazzucchelli, C., Carilli, C., Fan, X., Rix, H.-W., and Wang, R. (2020). Kiloparsec-scale ALMA Imaging of [C II] and Dust Continuum Emission of 27 Quasar Host Galaxies at z $\sim$ 6. , 904(2):130.

Verhamme, A., Schaerer, D., and Maselli, A. (2006). 3D Lyα radiation transfer. I. Understanding Lyα line profile morphologies. , 460(2):397–413.

Wise, J. H., Turk, M. J., Norman, M. L., and Abel, T. (2011). The birth of a galaxy: primordial metal enrichment and stellar populations. *The Astrophysical Journal*, 745(1):50.

Wolfire, M. G., McKee, C. F., Hollenbach, D., and Tielens, A. G. G. M. (2003). Neutral Atomic Phases of the Interstellar Medium in the Galaxy. , 587:278–311.

Yang, Y., Zabludoff, A., Jahnke, K., and Davé, R. (2014). The properties of lyα nebulae: gas kinematics from nonresonant lines. *The Astrophysical Journal*, 793(2):114.

Zitrin, A., Labbé, I., Belli, S., Bouwens, R., Ellis, R. S., Roberts-Borsani, G., Stark, D. P., Oesch, P. A., and Smit, R. (2015). Lymanα Emission from a Luminous z = 8.68 Galaxy: Implications for Galaxies as Tracers of Cosmic Reionization. , 810(1):L12.

Appendix A

NOEMA [CII] line observations of GN-108036

Fig. A0.1 shows the [CII] line spectra of GN-108036 (left) and the potential companion (right) extracted from the D, C, and combined array configuration data, respectively.

Fig. A0.2 shows the [CII] line integrated intensity map of GN-108036 based on the compact array (D) data. The contours correspond to 2.5, 3, 3.5, 4, 4.5, 5 and 5.5σ significance levels. The white cross at the center corresponds to the position of the HST rest-frame UV emission from GN-108036.

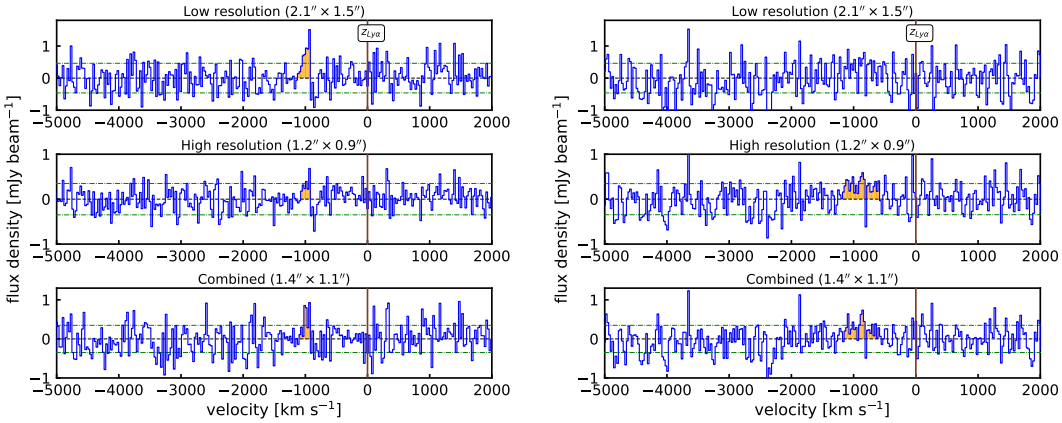

Figure A0.1: *Left:* NOEMA spectrum of GN-108036 with a possible new [CII] 158 μm transition detection (orange area). In all three panels, the green dotted line indicates the respective rms noise for three different data sets. Red solid line indicates the redshift measured by Lyα detection. *Right:* Same as the left panel but for the companion system.

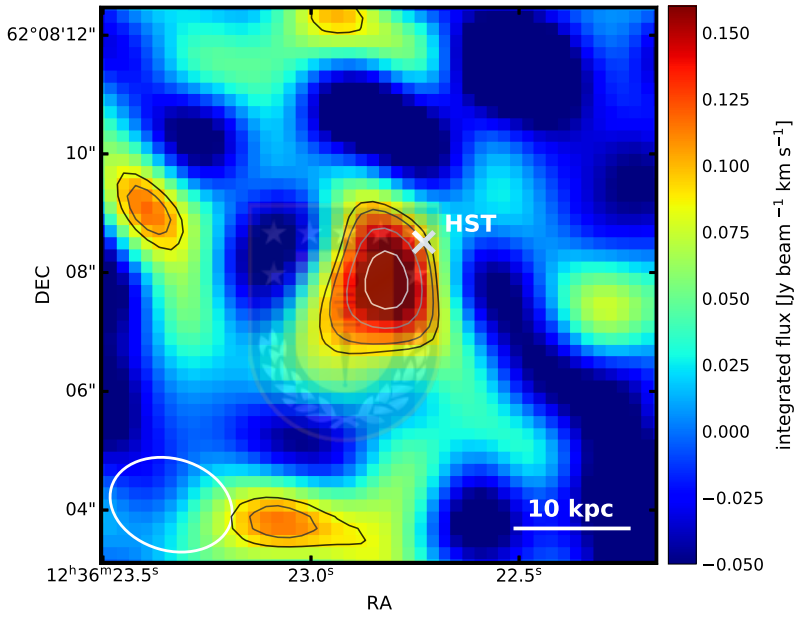

Figure A0.2: Flux map of GN-108036 in [CII] emission line for the compact data set. The contours corresponds to the 2.5σ, 3σ, 3.5σ, 4σ, 4.5σ, 5σ and 5.5σ (integrated) levels. The beam size is plotted in the bottom left.